MEMS based Optical Cross Connects for Fiber Optical Communication

Dissertation

submitted to the Faculty of Science of the University of Neuchatel, in fulfilment of the requirements for the degree of Doctor of Science

by

Michael Zickar

Institute of Microtechnology
University of Neuchatel
Switzerland

2006

Université de Neuchâtel

IMPRIMATUR POUR LA THESE

MEMS based Optical Cross Connects for Fiber Optical Communication

Michael ZICKAR

UNIVERSITE DE NEUCHATEL

FACULTE DES SCIENCES

La Faculté des sciences de l'Université de Neuchâtel,
sur le rapport des membres du jury

MM. N. de Rooij (directeur de thèse),
H.P. Herzig, W. Noell,
C. Marxer (Sercalo-Neuchâtel) et
H. Shea (EPF Lausanne)

autorise l'impression de la présente thèse.

Neuchâtel, le 16 mars 2006

Le doyen :

J.-P. Derendinger

■ Faculté des Sciences
■ Rue Emile-Argand 11 ■ CP 158 ■ CH-2009 Neuchâtel
■ Téléphone : +41 32 718 21 00 ■ Fax : +41 32 718 21 03 ■ E-mail : secretariat.sciences@unine.ch ■ www.unine.ch

Abstract

MEMS based optical cross connects experience a growing market demand. They are used in optical fiber networks as well as optical measurement systems where they add functionality or increase the performance of the systems. 2x2 MEMS optical cross connects proved excellent performance and large optical cross connects with over 100 input and output channels are used to route the worldwide data traffic. However, large optical cross connects have a high cost. Medium sized optical cross connects having four to sixteen input and output ports and moderate price clearly cover an industry need. Therefore, the subject of this thesis is the development of a matrix type optical cross connect with four or eight input and output ports. The pitch of the individual mirrors was set to 250 µm to enable a simplified assembly to fiber ribbons. A novel two-sided etching process of 110 µm thin silicon wafers enabled to fabricate silicon structures with a high accuracy on both sides of the wafer. The optical mirrors are situated vertically on very compact actuators with a footprint of 250 x 250 μm^2. The actuators consist of a fixed electrode and a counterelectrode suspended by torsion beams with a diameter of 0.8 µm. The simulation, fabrication and characterisation of microfabricated Graded Index lenses are presented. Theses lenses are needed to collimate the light exiting from the single-mode fibers, which is necessary to reduce losses originating from diffraction. The lenses are fabricated from a selected multi-mode fiber with a parabolic refractive index distribution in the fiber core. Since the diameter of the lenses equals the diameter of the signal carrying fibers they can be passively aligned in U-grooves that are etched into the silicon chip. The lenses yielded optical losses of less than 2 dB for a coupling length of 2 mm. The measurements of complete optical cross connects yielded encouraging results. The maximal operating frequency was measured to be larger than 200 Hz and the optical losses of some channels were close to the losses caused by the lenses, which means that the quality of the mirrors is good. However, some mirrors yielded losses that exceeded largely the targeted 3 dB. The reason was found to be the fragility of the silicon chip causing alignment problems after the assembly. A modification of the fabrication process allowing to fabricate more rigid mirror matrices is suggested.

Table of Contents

1 Introduction

1.1 The History of Communication

Communication is the most important interaction between human beings. We talk to interact with other people and to express what we think. Physically, talking is the emission of sound. The voice is transferred by the air through little pressure variations from the emitter to the receptor. The receptor is decoding the pressure variations into information. However, this kind of communication is restricted to a short distance between emitter and receptor. The desire to share information over long distances made people think about new technologies to transmit information. Already in the antiquity people used mirrors, fire or smoke signals to convey information over a long distance[1]. A first communication network based on this idea was suggested by Claude Chappe and realised between Paris and Lille in 1794; two cities about 200 km away[2]. The coded messages were transmitted using several intermediate relay stations. The drawback of this system was its low data rate and the dependency on the weather condition.

In 1832 F. B. Morse learned of Ampere's idea for electric communication. For the first time the coded information was guided through a communication channel, where the direction could be defined by the user.

The use of intermediate relay stations allowed communication over long distances and in 1866 the first Telegraph cable was crossing the Atlantic Ocean.

The success of the Telegraph was suddenly slowed down by the invention of the Telephone in 1876[3]. The invention by Alexander Graham Bell enabled not only the transmission of a simple content of information from an emitter to a receiver but the voice that was transmitted through the electrical cable could also express feelings and emotions. As a result, worldwide telephone networks were created during the 20th century. The use of the first coaxial cable in 1940 had the capability of transmitting 300 voice channels. The most advanced coax-cable was put into service in 1975 and was operated at 274 Mb/s. However, these high-speed coax-systems needed a repeater spacing of about 1 km, which was limiting further success.

Meanwhile, several researchers found that an optically dense medium could act as a light guide. Glass rods were used for transmission of light over short distances. However, the high losses and the lack of a coherent light source made glass unsuitable for optical communication. In 1960, Theodore Maiman invented the ruby laser and solved one part of the problem. Charles Kao and George Hockham postulated that the light loss in optical systems could be dramatically reduced by using amplifiers at intervals to amplify the signals[4]. Following on that postulation, research laboratories around the world tried to purify the optical materials in order to reduce fiber loss. In 1970, Robert Maurer, Donald Keck and Peter Schultz at Corning Inc. announced that they had made single-mode fibers with attenuation below 20 dB/km. The invention of the Erbium doped fiber amplifier in 1985 allowed the amplification of an optical signal without the need of electronical amplifiers. It was just a matter of time before the first transatlantic fiber cable was laid into the ocean in 1988.

Todays optical fibers carry up to 160 (and more) individual channels simultaneously resulting in data rates of several Tbit/s. To compare this value with the data capacity of a coax-cable one Tbit/s corresponds to the capability of transmitting about 15 million telephone lines in parallel. In the future, the perpetually growing internet traffic and the increasing demand of digital information as digital television and online multimedia applications will sustain the need for even faster communication lines.

1.2 General Description of Optical Networks

The concept of an optical network does not differ from any other communication network. A signal is modulated by the emitter and transferred through the communication channel to a receiver, where the signal is amplified, detected and demodulated. In the case of an optical network light is used as the signal carrying medium. A schematic of a simple optical network is given in figure 1.1. The light source is a laser or a light emitting diode (LED) that can be modulated electrically with high modulation frequencies[5]. This signal is injected into an optical fiber which guides the light at very high speed and low loss over long distances. On the receiver side the light is detected by a sensor and converted into an electrical signal again. After amplification, this signal is demodulated and can now be processed by electronic circuits.

Of course, one could use a copper wire instead of an optical fiber to transmit information without the use of optical transducers. However, optical communication has major advantages over electrical communication:

- The strongest argument for optical fibers is their information capacity. Where electrical coaxial cables have a transmission rate of 150 Mbps (million bits per second) corresponding to about 2000 digital telephone lines an optical fiber offers a transmission rate of 100 Gbps or more per

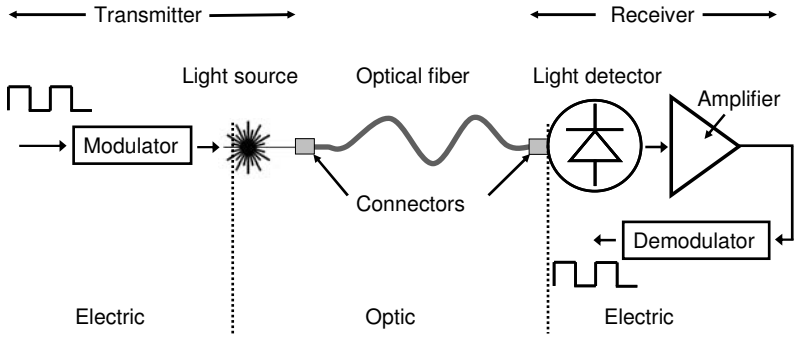

Figure 1.1: *Schematic of a simple optical network. A light signal is electrically modulated and transmitted through an optical fiber. The receiver converts the optical signal into an electrical signal, amplifies and demodulates it.*

transmission channel. Using a technology called dense wavelength division multiplexing (DWDM), 128 channels or more can be transferred using only one fiber resulting in a theoretical transmission rate of 12.8 Tbps. The theoretical limit of an optical fiber is 100Tbps. Long distance optical transmission lines (e.g. transatlantic optical cable TAT-14[6]) are operated at 10 Gbps carrying 16 channels in parallel resulting in a transmission rate of 160 Gbps or 2.5 million telephone lines in parallel.

- The distance between the signal repeaters, which amplify the attenuated signal, is typically 40 kilometers and considerably longer than the 12 kilometers needed for electrical communication. With the invention of the Erbium doped fiber amplifier (EDFA) light signals can be amplified optically without the need of conversion to electrical signals.
- The cost for a fiber cable is significantly lower than the price for a copper cable with the same transmission capacity.
- Other advantages including the elimination of a common electrical ground potential, better security, the insensitivity to magnetic fields, the small size and the light weight additionally favour the use of optical fibers.

As already mentioned, today's optical networks carry more than one light channel per fiber. The WDM (wavelength division multiplexing) technique enables the transmission of multiple wavelengths in one fiber without any interaction. The data rate of the fiber is multiplied by the number of wavelengths injected in the fiber. The so called C-band (Conventional band) situated at a wavelength range of 1520 to 1570 nm can be split in 64 or even 128 individual channels[7]. To couple multiple wavelengths simultaneously

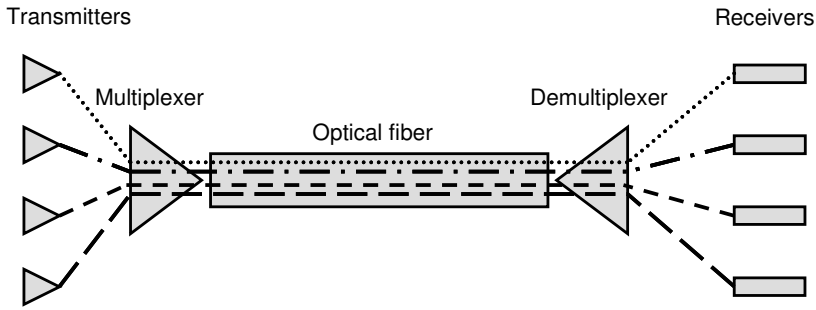

Figure 1.2: *Schematic of an optical network using WDM technique. Four light channels with slightly different wavelengths are coupled into the same optical fiber and transmitted without interaction.*

into and out of the same fiber, two additional optical elements called multiplexer and demultiplexer have to be integrated (see figure 1.2).

1.3 MEMS in Optical Networks

The first optical networks used electro-optical transducers and analog electronics to process the signals electrically before regenerating an optical signal with a light source and reinjecting the signal into another optical fiber. These networks are called optical-electrical-optical (OEO) networks. The advantages of optical signal processing towards electronic processing, pointed out in the previous chapter, raised a big interest in all optical networks (OOO networks). The small dimension of light exiting a telecom fiber requires very small and precise equipment that needs to be perfectly aligned to the fiber. Optical micro electro-mechanical systems (OMEMS) fulfil these requirements. A big research activity in the MEMS field was launched in the late 80's and is still going on. Since then, many OMEMS found their place in optical networks and replaced conventional micro-optical elements or enabled new functionality to the networks. Some examples are briefly presented hereafter.

- Tunable filters:
  Optical filters can be used as multiplexers. The desired wavelength of the superimposed WDM signal passes the optical element whereas the other wavelengths are reflected. By cascading such filters, the different wavelengths can be separated (demultiplexed). The requirements for WDM multiplexers are high wavelength selectivity in the order of 1 nm, low insertion loss and low temperature dependency. Whereas thin film filters can be fabricated with sophisticated deposition processes, tunable MEMS devices are under large development[8,9,10,11,12].
  Due to the relatively high insertion loss per filter stage this method is only suitable for a small number of channels.

- Tunable gratings:
  As in the case of optical filters, the functionality of gratings is enhanced by adding a tuning mechanism[13] to be used as an optical filter.

- Variable attenuators:
  It does not seem logical to add an attenuating element into an optical network. However, one has to understand that the amplification of the WDM signals is carried out with special optical fibers called Erbium doped fiber amplifiers (EDFA). Their amplification factor is not the same for all the wavelengths in the WDM bandwidth. The function of a variable attenuator is to equalize the signals to a common intensity level before being injected into the transmission fiber. The quality of an attenuator is measured by its attenuation range, its resolution and the insertion loss. MEMS attenuators can be divided into two groups: Shutter type and reflective attenuators. Shutter type attenuators are operated in transmission and use a light blocking element (shutter) that blocks a part of the light beam[14,15]. A very precise positioning of the shutter yields the required high resolution. Dynamic attenuation ranges up to 60dB were reported.
  Reflective attenuators use movable mirrors to steer the incoming light beam. If the mirror is actuated the light beam is reflected in a way that only a part of the light is coupled into the outgoing fiber. Analog[16] as well as digital designs[17] were reported.

- Optical cross connects:
  To send a packet of information to a desired destination it has to take the right path. In all optical networks the switching is accomplished by small mirrors that route the light beam from an input to any output fiber. Many designs for MEMS optical switches have been proposed. They can be categorized in two-dimensional (2D) and three-dimensional (3D) switches. 2D architectures have been successfully fabricated and proved to have excellent reliability, which allowed commercialization[18,19].

1.4 Microlenses

The small nature of light beams, which are guided in Telecom single mode fibers, make relevant several optical effects that are negligible in the macro-world. Due to high divergence angles of small optical beams the optical losses increase drastically if the light beam has to travel over a long distance. Microlenses enable the beam waist to be broadened and increase the coupling length between two waveguides.

The compatibility of an optical element to a MEMS device is defined by its dimensions and the accuracy with which it can be aligned to the microchip. Optical fibers are widely used to guide light to a very well defined place on an OMEMS. They can be aligned to the optical element using U- or V-grooves etched into the MEMS device. In an ideal case the grooves are etched during the same step as the optical element itself, which enables a passive alignment of the optical components with very high accuracy[20,21]. The light beam emerging from a typical single mode fiber (SMF) has a mode field diameter of about 10 µm[22]. The high diffraction angle of this beam allows free space propagation over only several tens of micrometers where the light can be processed before being coupled into another waveguide. This is only suitable for very thin optical components as vertical optical mirrors, optical attenuators or thin film filters[23]. For longer free space propagation the beam waist has to be broadened using collimating lenses.

Different fiber-lens systems have been proposed. The shape of a classical refractive lens is ideally a radial hyperbolic function resulting in different optical path lengths along its radius due to the varying thickness of the material. These lenses can be fabricated by reflowing patterned photo-resist shapes on a transparent substrate. The lens shape of the photo-resist can be transferred into the substrate using dry etching techniques, usually into silicon or glass[24]. Printing technologies have been reported using microjets to control the amount of dispensed liquid thus controlling the shape of the lens[25].

Another technique to create an optical path difference along a lens is changing its refractive index in radial direction. Planar lenses can be fabricated by ion exchange technique in glass where a radial refractive index variation is achieved by molecular diffusion[26,27].

An inconvenience for all planar lenses is the difficult assembly to optical fibers or microchips. Due to their planar nature it is difficult to integrate passive alignment structures. Particularly angular misalignments are very likely.

Ball lenses are transparent balls assembled to a chip. Ball lensed fibers are fabricated by heating the tip of an optical fiber. The surface tension of melted glass forms a ball lens directly attached to the fiber[28].

Cylindrical micro-lenses consist of a rod of transparent material with a graded refractive index (GRIN) profile in radial direction. The length of these rods defines the focal distance of the lens. Optical multi-mode fibers (MMF) with GRIN core are commercial products. If such a GRIN fiber is fusion spliced to a single mode fiber (SMF), cut and polished to a desired length the result is a lensed fiber[29]. This method leaves a little bead at the splicing area.

Diffractive microlenses with a lens diameter of 125 µm were reported[30].

In conclusion, all these lenses suffer from their non-uniform lateral dimension, which makes it difficult to align them to optical fibers. Additionally, their fabrication is complicated, needs a clean-room environment or they can not be fabricated in parallel causing a high production cost per piece.

Ideally, a microlens that is assembled onto a microchip has the same shape as the light carrying optical fiber. Under this condition the lens and the optical fiber can be placed in the same U- or V-groove and are passively aligned.

1.5 Motivation and Outline of the Thesis

As explained in section 1.2, in an optical network optical signals need to be switched (or routed) from a transmitter to the desired receiver. An all optical method of optical switching can be achieved by precisely operating an optical mirror and reflecting the light beam escaping the incoming optical fiber into the desired outgoing fiber.

MEMS optical switches can be categorized in two-dimensional (2D) and three-dimensional (3D) switches. As mentioned earlier, 2D architectures have been successfully fabricated and proved excellent reliability. The advantage of these designs is that the mirrors are either made by silicon bulk micromachining or poly-silicon surface micromachining where the mirrors do not have to be assembled to the actuators. Surface micromachining needs hinged micro-mirrors made of poly-silicon. These mirrors are flipped-up planar mirrors, where multiple mask fabrication is required. The mounting of the mirrors needs sophisticated and complicated processes, often even manual help. Bulk micromachined, KOH etched[31] vertical mirrors, which are moved in and out of the optical path are easier to control. Because the mirror remains within the switching/reflecting plane, a small change in actuation does not result in a large change of optical coupling. However, these relatively large mirrors are difficult to fabricate and yield long optical coupling distances. The mirrors are fabricated on cantilevers, which is space consuming. Horizontal mirrors[32,33] need to have mechanical stoppers to align them vertically, which need to be perfectly perpendicular to the light beam plane. Mechanical contact of microstructures can provoke sticking and breaking of the fragile mirror.

Mounting mirrors on actuators is a difficult task since the alignment needs to be in the range of a micrometer. SU-8 mirrors on silicon actuators have been reported[34] but the long term adhesion of the two parts have yet to be

proven. One way to overcome the free space propagation of light is the use of waveguides[35,36]. The light beam is confined in a medium with a high refractive index and only propagates in free space for a very short path length around the mirror to keep diffraction losses small.

3D switches offer a high number of input and output ports. They consist of a matrix of planar 2D mirrors that can be tilted independently to redirect an incoming beam to any other mirror on either another[37,38,39] or the same[40] mirror matrix. The latter enables any port to be configured as input or output. Two or more mirrors can redirect a beam into one output, in order to add light channels to an optical fiber. However, these mirrors need a closed loop control, calibration, a precise housing to align the chips and the collimators. Additionally, the large optical paths require large optical beams thus large mirrors.

The principle for a 2x2 2D optical cross connect (OXC) is shown in figure 1.3. A microfabricated vertical mirror is driven by an electrostatic comb drive actuator. Such an optical MEMS switch was realised at IMT in 1998 and commercialised by Sercalo inc. (figure 1.4)[41].

The need for larger port count optical cross connects was the initiator for this project. The aim was to fabricate a compact 4x4 and 8x8 2D matrix OXC having the same pitch as the neighbouring fibers in commercially available fiber ribbons. This allows an economic assembly of the fiber ribbons to the chip but limits the space for the used actuator to 250 x 250 μm^2. Since the size of electrostatic comb drive actuators exceeds this

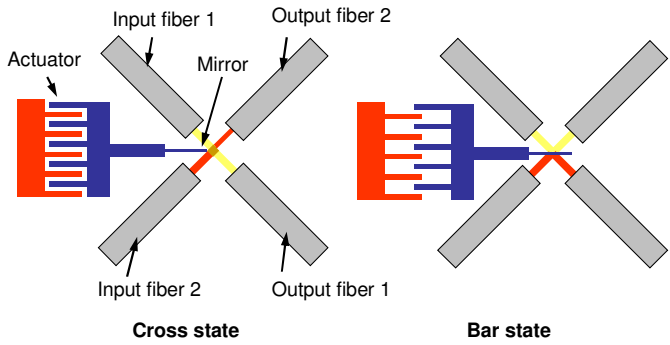

Figure 1.3: *Principle of a 2x2 optical cross connect. A vertical mirror is positioned with an electrostatic comb-drive actuator. Depending on the mirror position a light beam can be redirected into the desired output fiber.*

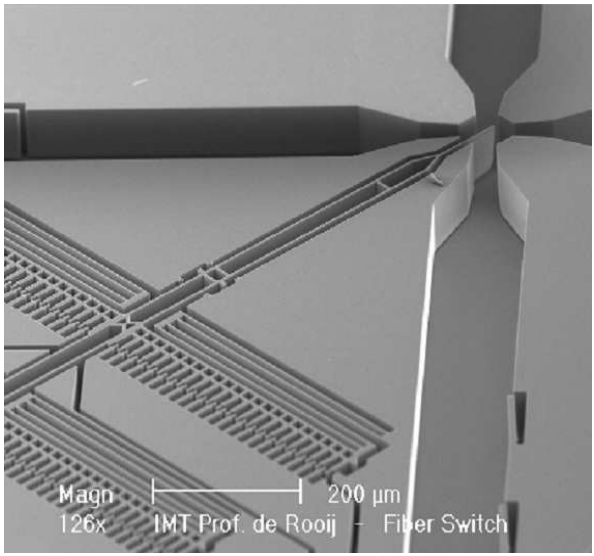

Figure 1.4: *SEM image of a 2x2 optical cross connect commercialised by Sercalo Inc.*

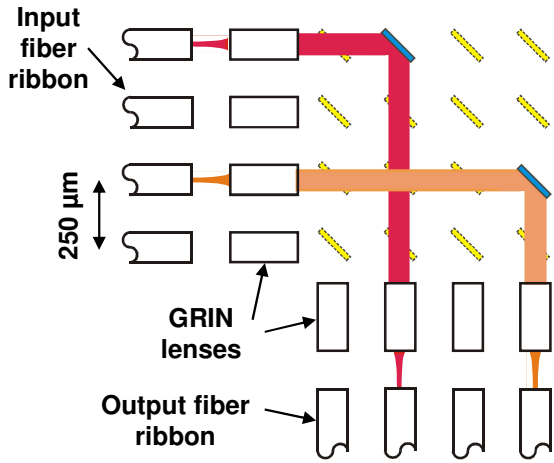

Figure 1.5: *Conceptual drawing of a 4x4 matrix OXC: The device consists of a mirror matrix with a pitch of 250 µm, assembled fiber ribbons and GRIN lenses.*

dimensions a novel out-of-plane actuator with 1 µm diameter torsion beams, on which a vertical mirror was monolithically etched, was developed and characterized. Novel micro-GRIN lenses were simulated, fabricated, characterized and found to be suitable to collimate the light on the 4x4 and 8x8 OXC. A conceptual drawing of the design is shown in figure 1.5.

The outline of the thesis is as follows: The theory part presents an overview about mechanical and optical simulation techniques, which will be used to model and design the MEMS chip and micro-optical components. An electro-mechanical simulation strategy for the calculation of large out-of-plane movements of electrostatic actuators is presented and verified. The actual dimensioning and tolerancing is presented in the concept chapter. Chapter 4 shows the technological realisation of the MEMS actuator, the electrode chip and the micro GRIN lenses. A big part of this chapter presents the assembly of the chip and the driving electronics, which supplies a voltage of about 400 V to the 64 actuators. The measurements of the electromechanical performance of the MEMS part, the optical coupling losses of the lenses and the performance of the assembled OXC are shown and discussed in the chapter 5. Finally, the conclusion is drawn in chapter 6.

References:

[1] G. J. Holzmann and B. Pehrson, “The early History of Data Networks“, IEEE Computer Society Press, Los Alamitos, CA, 1995.

[2] G. P. Agrawal, “Fiber-Optic Communication Systems“, John Wiley & Sons Inc., 2002.

[3] A. B. Bell, U.S. Patent No. 174,465 (1876).

[4] K. C. Kao, G. A. Hockham, Proc. IEE 113, 1151 (1966).

[5] Harry J. R. Dutton, “Understanding Optical Communications”, IBM Redbook, 1998.

[6] Webpage: https://www.tat-14.com

[7] Webpage: http://www.cisco.com/univercd/cc/td/doc/product/mels/cm1500/dwdm/dwdm_ovr.htm

[8] X. Li, R. Belikov, K. Yu, O. Solgaard, “Micromachined Tunable Blazed Gratings”, OMEMS 2004, Takamatsu, pp. 6-7.

[9] T. Overstolz, G. Niederer, W. Noell, H. P. Herzig, S. Obi, H. Thiele, M. T. Gale, N. F. de Rooij, “MEMS Tilting Platform for Filter Tuning in Optical Telecom, OMEMS 2004, Takamatsu, pp. 10-12.

[10] D. Hohlfeld, H. Zappe, “A MEMS-based All-dielectric Tunable Optical Filter with Incresed Tuning Range”, Photonics Europe 04, Proc. of SPIE, Vol. 5455, pp. 228-239.

[11] P. Meissner, M. Aziz, H. Halbritter, F. Riemenschneider, “Micromachined Two-Chip Filters for WDM Transmission Systems“, OMEMS 03, Lugano, pp. 167-168.

[12] A. Tarraf, J. Daleiden, F. Römer, C. Prott, V. Ragelov, S. Irmer, E. Ataro, H. Hillmer, “A Nover Low-cost Tunable Dielectric Air-gap Filter“, OMEMS 03, Lugano, pp. 175-176.

[13] T. Kimura, N. Fujimura, N. Kanbara, “Wide Range Tunable Filter Module based on MEMS Tilt Mirror”, OMEMS 04, Takamatsu, Japan, pp. 12-13.

[14] C. Marxer, P. Griss, and N. F. de Rooij, “A variable optical attenuator based on silicon micromechanics,” IEEE Photon. Technol. Lett., vol. 11, pp. 233–235, Feb. 1999.

[15] R. R. A. Syms, H. Zou, J. Stagg, and D. F. Moore, “Multistate Latching MEMS Variable Optical Attenuator”, IEEE Photonics Technology Letter, Vol. 16, No. 1, 2004.

[16] K. Isamoto, A. M., M. Tei, H. Fujita and H. Toshiyoshi, “A 5-volt operated MEMS variable optical attenuator by SOI bulk micromachining”, IEEE J. Selected Topics in Quantum Elec (JSTQE), vol. 10, No. 3, May-June 2004, pp. 570-578.

[17] W. Sun, J. Mughal, F. Perez, N. Riza, W. Noell, N. F. de Rooij, ”Design and Fabrication of a Circular Digital Variable Optical Attenuator”, Photonics Europe 04, Proc. of SPIE, Vol. 5455, pp. 220-227.

[18] C. Marxer, C. Thio, M. Grétillat, N. F. de Rooij, R. Bättig, O. Anthamatten, B. Valk, P. Vogel, “Veritcal mirrors fabricated by deep reactive ion etching for fiber-optic switching applications”, JMEMS Vol. 6, No. 3, 1997, pp. 277-285.

[19] Shi-Sheng Lee, Long-Sun Huang, Chang-Jin Kim, Wu MC, “2*2 MEMS fiber optic switches with silicon sub-mount for low-cost packaging”, Solid-State Sensor and Actuator Workshop. Transducers, 1998, pp.281-4. Cleveland, OH, USA.

[20] W. Noell, P-A. Clerc, L. Dellmann, B. Guldimann, H.P. Herzig, O. Manzardo, C. Marxer, K. Weible, R. Dändliker, N. de Rooij, “Applications of SOI-based optical MEMS”, IEEE Journal on Selected Topics in Quantum Electronics, vol. 8, NO.1, 2002, pp. 148-154.

[21] H. Toshiyoshi, H. Fujita, “Electrostatic Micro Torsion Mirrors for an Optical Switch Matrix”, Journal of Microelectromechanical Systems, IEEE, vol.5, no.4, Dec. 1996, pp.231-7, USA.

[22] Corning SMF-28 product information.

[23] C. Marxer et, C. Thio, M-A. Gretillat, N. de Rooij, R. Bättig, O. Anthamatten, B. Valk, P. Vogel, “Vertical Mirrors Fabricated by Deep Reactive Ion Etching for Fiber-Optic Switching Apllications”, JMEMS Vol. 6, No. 3, 1997, pp. 277-285.

[24] Ph. Nussbaum, R. Völkel, H.P. Herzig, M. Eisner, S. Haselback, „Design, Fabrication and Testing of Microlens Arrays for Sensors and Microsystems“, Pure Appl. Opt. 6, 1997, pp. 617-636.

[25] W. R. Cox, C. Guan, D. J. Hayes, “Microjet Printing of Micro-optical Interconnects and Sensors”, SPIE Phot. West Proc., V.3852, 2000, p. 400.

[26] J. Bähr, U. Krackhardt, K.-H. Brenner, “Fabrication and Testing of planar Micro Lens Arrays by Ion Exchange Technique in Glass”, SPIE-Int. Soc. Opt. Eng. Proceedings of Spie, vol.4455, 2001, pp.281-92. USA.

[27] F. Zhu, Y. Sato, Y. Sasaki, K. Hamanaka, “Fiber Collimator Arrays for Optical Devices/Systems”, Proc. of SPIE, Vol. 4564, 2001, pp. 175-182.

[28] Corning Product Information: www.corning.com

[29] Patent: US4701011, “Multimode fiber-lens optical coupler” 1987.

[30] Webpage: http://www.oki.com/en/press/2002/z02062e.html

[31] M. Mita, P. Hélin, D. Miyauchi, H. Toshiyishi, H. Fujita, “Optical and surface characterisation of poly-Si replica mirrors for an optical fiber switch”, Transducers 1999, Sendai, Japan.

[32] Toshiyoshi H, Fujita H., “Electrostatic micro torsion mirrors for an optical switch matrix”, Journal of Microelectromechanical Systems, vol.5, no.4, Dec. 1996, pp.231-7.

[33] Houlet L, Reyne G, Bourouina T, Yasui M, Hirabayashi Y, Ozawa T, Okano Y, Fujita H, "Design and realization of magnetic actuators for optical matrix micro-switches", IEEE/LEOS International Conference on Optical MEMS, 2002, pp.113-14. Piscataway, NJ, USA.

[34] Liu Suyan, Bu Minqiang, Ye Xiongying, Zhou Zhaoying, Zhang Dacheng, Li Ting, Hao Yilong, Tan Zhimin, "Micromachined optical switch with a vertical SU-8 mirror", SPIE-Int. Soc. Opt. Eng. Proceedings of Spie - the International Society for Optical Engineering, vol.4601, 2001, pp.354-9. USA.

[35] Dellmann L, Noell W, Marxer C, Weible K, Hoffmann M, de Rooij NF, "4*4 matrix switch based on MEMS switches and integrated waveguides", TRANSDUCERS 2001, pp.1332-5 vol.2. Berlin, Germany.

[36] Ollier E, Divoux C, Margail J, Enot T, Oritz L, Gobil Y, Salhi M, Berruyer P, Glière A, Bontemps A, "Electrostatically actuated micro-fluidic optical cross-connenct switch", Int. conf. on optical MEMS, 2003, Hawaii, pp. 47-48.

[37] Sawada R, Yamaguchi J, Higurashi E, Shimizu A, Yamamoto T, Takeuchi N, Uenishi Y, "Single Si crystal 1024ch MEMES mirror based on terraced electrodes and a high-aspect ratio torsion spring for 3-D cross-connect switch", Int. conf. on optical MEMS, 2002, Lugano, pp. 11-12.

[38] Yamamoto T, Yamaguchi J, Sawada R, Uenishi Y, "Development of a Large-scale 3D MEMS optical switch module", NTT technical review, vol. 1, No. 7, Oct. 2003.

[39] Kouma N, Tsuboi O, Mizuno Y, Okuda H, Xiaoyu M, Iwaki M, Soneda H, Ueda S, Sawaki I, "A 2- axis comb-driven micromirror array for 3D MEMS switches", conf. on optical MEMS, 2003, Hawaii, pp. 53-54.

[40] http://www.elecdesign.com/Articles/Index.cfm?ArticleID=5942

[41] C. Marxer, C. Thio, M-A. Gretillat, N. de Rooij, R. Bättig, O. Anthamatten, B. Valk, P. Vogel, "Vertical Mirrors Fabricated by Deep

Reactive Ion Etching for Fiber-Optic Switching Applications", JMEMS Vol. 6, No. 3, 1997, pp. 277-285.

2 Theory

2.1 MEMS Actuators

The functionality of many MEMS is driven by its micromachined actuators. Different actuation concepts have been reported. Among those are Piezo-electric[1], thermal, magnetic[2] and electrostatic actuators. Electrostatic actuators have some considerable advantages. The most important are their small dimensions. If a voltage is applied between two electrically isolated parts then electrostatic forces in the micro-Newton range are generated and act on the parts. An advantage of silicon actuators is that they are not sensitive to magnetic fields.

Parallel plate actuators are simple to fabricate but their usable stroke is limited to one third of the initial displacement by the so called "pull-in" effect[3]. An enhanced design is the comb-drive actuator where a movable comb electrode is attracted towards a fixed comb electrode (see figures 1.3 and 1.4). The stroke is then defined by the length of the comb-fingers and the lateral stability of the movable structure. Strokes over 100 µm have been demonstrated[4]. Actuators based on repulsive electrostatic force have been recently reported[5,6].

The dimensioning of electrostatic actuators is calculated by analytical calculations of electrostatic and mechanical force or by using the Finite Element Method (FEM). Both methods are very well suited for actuators that

move only in one linear direction or for small displacements. For large out-of-plane movements, FEM algorithms have a tendency to fail. Therefore, a simulation concept for large deflection tilting platforms, which combines electrostatic FEM simulation and analytical calculation of the mechanical springs, is presented hereafter. Since the electro-mechanical characteristic of the actuator is calculated by means of the electrostatic energy this method will be referred as the "energy method".

2.1.1 Combined FEM and Mechanical Simulation Method for Large Deflection Actuators (Energy Method)

The results of coupled FEM simulations for large mechanical deflection electrostatic actuators are often unsatisfying. Additionally, the simulation time increases drastically with the complexity of the structure and the number of mesh nodes.

The energy method, presented hereafter, is very fast and showed surprisingly accurate results. However, it can only be used if the approximate mechanical behaviour of the actuator is known. The principle will be explained and verified using the simple example of a parallel plate actuator, shown in figure 2.1. The bottom plate is fixed and the top plate is held in vertical position by springs with spring constant k. The first step is to perform an electrostatic FEM simulation for several positions the device is thought to move to. For these positions the electrostatic energy of the whole system is calculated. This task can be very easily implemented in ANSYS and is not sensitive to variations of the mesh model. In our case, we simulated the capacity for several plate separations. The electrostatic energy is related to the capacity of the system by

$$E_{ES}(d,V) = \frac{1}{2}C(d)V^2 . \tag{2.1}$$

The mechanical potential energy of the spring is given by

$$E_{Mec}(d) = \frac{1}{2}kd^2 . \tag{2.2}$$

Our movable plate will stabilize in the position where the electrostatic force equals the counterforce generated by the spring. The corresponding forces can be calculated by the derivates of the energies:

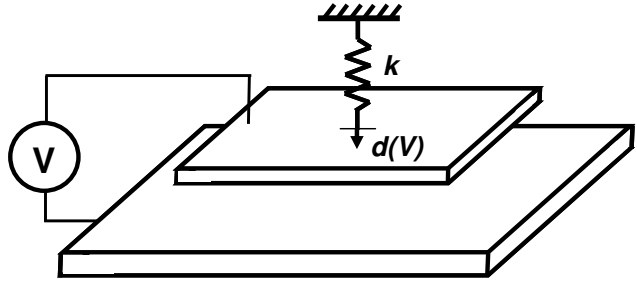

Figure 2.1: *Parallel plate actuator suspended by a linear spring having a spring constant k. If a voltage is applied between the two conductors the upper, mobile plate moves towards the fixed lower plate.*

$$F_{ES} = \frac{\partial E_{ES}}{\partial d} \tag{2.3}$$

$$F_{Mec} = \frac{\partial E_{Mec}}{\partial d}. \tag{2.4}$$

This means that the plate is in a stable position if the variations of the mechanical and electrostatic energies are equal. For the case of the electrostatic energy the variation is caused by the increase of the capacity.

The mechanical force only depends on d whereas the electrostatic force depends on d and the applied voltage. From equations 2.1 and 2.3 it can be seen that the electrostatic force increases with V^2. Therefore, if the energy-displacement curve is known for one voltage it can be calculated for any other voltage.

To find the relation $d(V)$ we have to find the points where the difference between electrostatic and mechanical force equals zero.

$$F_{ES}(d,V) - F_{Mec}(d) = 0 \tag{2.5}$$

This can be solved graphically by plotting the difference between electrostatic and mechanical energy in function of d and V (Figure 2.2). The intersection with the d-V plane gives the relation between displacement and actuation voltage.

The big advantage of this method is that the FEM simulation of the electrostatic energy of a volume containing different electrodes is much simpler than the simulation of the forces that act between the charged electrodes.

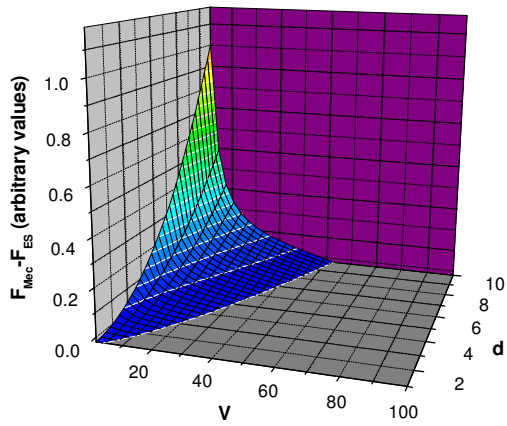

Figure 2.2: *Difference between electrostatic and mechanical force for an electromechanical system: The intersection with the d-V plane gives the relation between displacement and actuation voltage.*

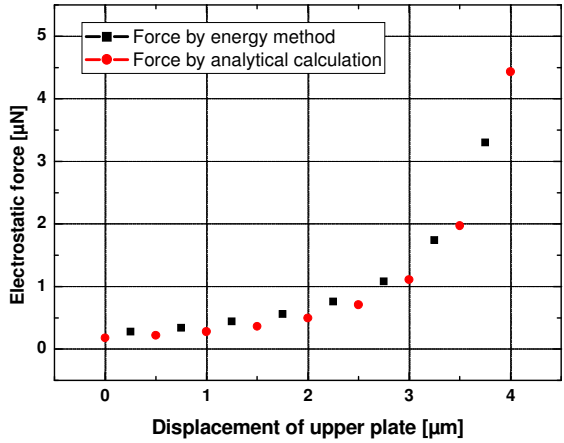

Figure 2.3: *The comparison between the forces calculated by the energy method and the analytical calculation for a parallel plate capacitor. The energy method yields slightly higher values, which is due to the edge effects that are not taken into account in the analytical calculation.*

The analytical equation solving the parallel plate capacity problem is

$$F_{ES} = \frac{\varepsilon_0}{2}\frac{V^2}{d^2}A \tag{2.6}$$

where A is the area of the movable electrode. To validate the energy method the comparison of the analytical calculation and the coupled simulation is shown in figure 2.3. The simulated force is slightly higher than the force obtained by the analytical calculation. This is due to the fringing fields on the edges of the capacitor that are only taken into account for the simulated (using equations 2.1 and 2.3) model (figure 2.4). The analytical model neglects edge effects.

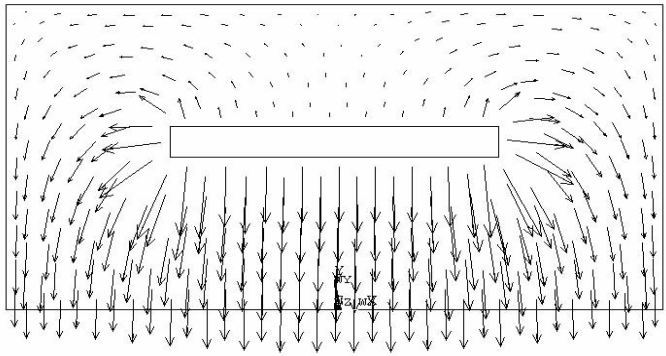

Figure 2.4: *FEM model (ANSYS) used to calculate the electrostatic energy of the actuator. The upper platform is visible in the middle of the image, the fixed platform is on the bottom. Plotted is the electric field.*

2.2 Optics

This chapter describes the optical elements that will be used in the OXC. The optical beam that is guided in an optical fiber used for communication networks can be approximated by a Gaussian profile. A simple mathematical model, called the ABCD method, is shortly introduced. This method allows us to calculate the evolution of Gaussian beam waists and radii of curvature for the paraxial case.

2.2.1 Optical Fibers

Optical fibers can be divided into two classes: Step index fibers consist of a fiber core and a surrounding cladding. The refractive index of the core is slightly higher. Paraxial light rays in the core are totally reflected at the boundary keeping the light confined in the core (figure 2.5 a)). The second class is graded index fibers, which have a core with a parabolic distribution of the refractive index (figure 2.5 b)). It can be expressed by

$$n(r) = \sqrt{n_0^2 (1 - \alpha^2 r^2)} \tag{2.7}$$

where n_0 is the refractive index in the centre of the fiber, r is the distance from the centre and α is the parabolic constant. The trajectory of a paraxial ray entering a GRIN core is a sinusoidal oscillation with a pitch of $2\pi/\alpha$.

If the GRIN material is cut at a certain length d it can act as a lens with desired focal distance. For an incoming plane wave the GRIN lens has a focal length of

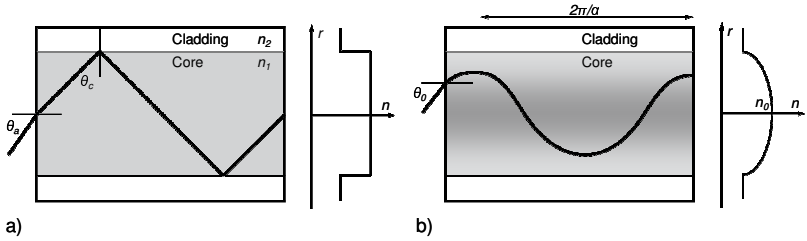

Figure 2.5: *Trajectory of a ray and refractive index distribution of a step-index fiber a) and a GRIN fiber with parabolic index distribution b).*

$$f \approx \frac{1}{n_0 \alpha \cdot \sin(\alpha d)} . \tag{2.8}$$

2.2.2 Micro-GRIN Lenses as Optical Collimators

The furthermost usage of micro-lenses on a chip is light collimation. In order to have larger free space coupling lengths the incoming beam waist has to be broadened. A broader beam waist has a smaller divergence angle, θ_0 ($\theta_0 = \lambda/\pi\omega_0$) therefore, a double diameter yields a four times higher coupling length having the same losses[7]. A schematic of the investigated arrangement is shown in figure 2.6. A light beam emerging from the SMF1 is collimated by GRIN lens 1, travels through the free space region and is refocused by GRIN lens 2 into the outgoing SMF 2.

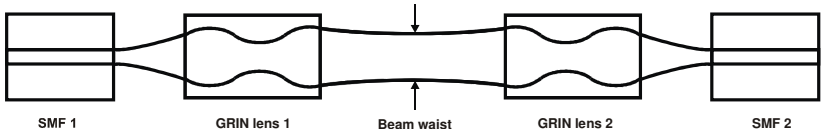

Figure 2.6: *Schematic of the collimating setup. A light beam emerges from the SMF and is collimated by GRIN lens 1. GRIN lens 2 refocuses the beam into the other SMF.*

2.2.3 Gaussian Beams and Beam Propagation

Gaussian beams are a paraxial solution to the wave equation[9]. The complex envelope of the Gaussian beam is given by

$$A(r) = \frac{A_1}{q(z)} \exp(-ik \frac{x^2 + y^2}{2q(z)}) \tag{2.9}$$

where A_1 is a constant z is the beam propagation axis, x and y are the plane perpendicular to the propagation axis and $q(z) = z + iz_0$. $q(z)$ is called the complex curvature parameter. The complex amplitude E has the form

$$E(x,y,z) = \frac{q_0}{q(z)} \exp(ikz) \exp(i \frac{k(x^2+y^2)}{2q(z)}) \tag{2.10}$$

with

$$q_0 = -i \frac{k\omega_0^2}{2} = -iz_0 \tag{2.11}$$

where z_0 is known as the Rayleigh Range and

$$q(z) = q_0 + z \,. \tag{2.12}$$

The real and imaginary part (amplitude and phase) of the complex curvature parameter can be separated by writing $1/q(z) = 1/(z + jz_0)$ and by defining two new real constants $R(z)$ and $\omega(z)$. The fundamental-mode Gaussian beam can now be described with the q parameter where its Gaussian beam spot size is represented by $\omega(z)$ and its radius of curvature is given by $R(z)$.

$$\frac{1}{q(z)} = \frac{1}{R(z)} - i \frac{\lambda}{\pi n_j \omega(z)^2} \,. \tag{2.13}$$

n_j is the refractive index of the medium in which the Gauss beam is propagating. The shape and the important parameters of a Gauss beam are shown in figure 2.7.

The parabolic constant can be expressed by

$$\alpha \approx \frac{NA}{n_0 r_{core}} \tag{2.14}$$

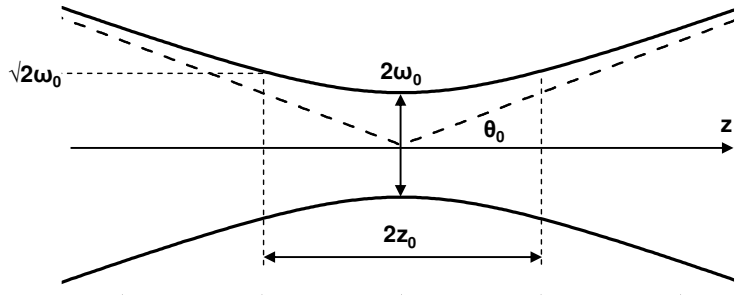

Figure 2.7: *Characteristics and important parameters of a Gauss beam.*

where NA is the numerical aperture of the lens and r_{core} is the radius of the GRIN lens core.

2.2.4 ABCD law

A convenient way for calculating paraxial rays in an optical system is the *ABCD* matrix method[8]. The basic principle of this approach is to split the system in a number of regions with a known *ABCD* matrix. For each region the coordinates x (radial position of the ray) and u (normalized slope) of the output can be related to the coordinates of the input by means of a matrix characterizing the system:

$$\begin{pmatrix} x_{out} \\ u_{out} \end{pmatrix} = \begin{pmatrix} A & B \\ C & D \end{pmatrix} \begin{pmatrix} x_{in} \\ u_{in} \end{pmatrix}. \tag{2.15}$$

Such a transfer matrix is called the *ABCD* matrix. For the given problem a number of different matrices are used.
For a homogeneous medium the matrix is defined as

$$\begin{pmatrix} A & B \\ C & D \end{pmatrix} = \begin{pmatrix} 1 & d \\ 0 & 1 \end{pmatrix} \tag{2.16}$$

where d is the geometrical length along the z-axis. For a discontinuity between two plane dielectrics

$$\begin{pmatrix} A & B \\ C & D \end{pmatrix} = \begin{pmatrix} 1 & 0 \\ 0 & \dfrac{n_1}{n_2} \end{pmatrix} \tag{2.17}$$

where n_1 is the refractive index of the input medium and n_2 is the refractive index of the output medium. Finally, a GRIN lens can be represented by

$$\begin{pmatrix} A & B \\ C & D \end{pmatrix} = \begin{pmatrix} \cos(\alpha Z) & \dfrac{1}{\alpha}\sin(\alpha Z) \\ -\alpha \sin(\alpha Z) & \cos(\alpha Z) \end{pmatrix} \tag{2.18}$$

where Z is the length of the GRIN lens. By multiplying the transfer matrices we can obtain the description of the whole system.

The complex curvature parameter q is altered by the optical system as

$$q_{j+1} = \frac{Aq_j + B}{Cq_j + D} \tag{2.19}$$

where j is the index for the corresponding medium. Because the q parameter identifies the width ω and curvature R of a Gaussian beam, this simple law allows us to calculate the effect of an arbitrary paraxial system on the Gaussian beam.

3.1.2 Beam Clipping

The definition of the beam waist for Gauss beams is given by the radial position where the intensity of the Gauss beam drops to the value of $1/e^2$ of the intensity in the spot centre. Theoretically, the intensity of a Gauss beam extends to an infinite plane perpendicular to the propagation direction. The intensity inside the $1/e^2$ circle comprises only 91% (-0.41 dB) of the whole intensity (figure 2.8). The consequence for our mirrors is that even if its dimension is bigger than the actual beam waist a small amount of light will

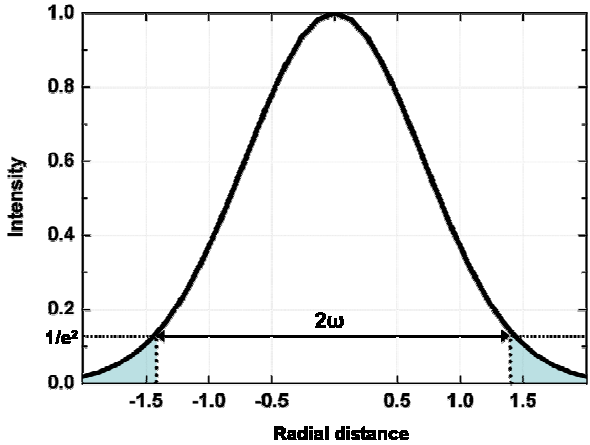

Figure 2.8: *Gaussian beam profile: Theoretically, a Gauss beam has an infinite extension perpendicular to its propagation axis. The beam waist diameter calculated by the Gaussian beam propagation theory is taken at the radial extension where the intensity of the beam drops to the factor of $1/e^2$ of the intensity in the beam centre.*

not be reflected, which will result in a contribution to the coupling loss. This effect is called beam clipping. If we take a round mirror with the same diameter as the reflected beam waist ω only 91% of the intensity will be reflected. In the worse case the mirror is smaller than the actual beam size causing a higher contribution to the coupling loss.

2.2.6 Coupling Efficiency

The coupling efficiency η is calculated by the so-called "overlap integral" as

$$\eta = \frac{\left| \int_{-\infty}^{\infty} \int_{-\infty}^{\infty} E_i(x,y) E_f^*(x,y) dxdy \right|^2}{\int_{-\infty}^{\infty} \int_{-\infty}^{\infty} E_i(x,y) E_i^*(x,y) dxdy \int_{-\infty}^{\infty} \int_{-\infty}^{\infty} E_f(x,y) E_f^*(x,y) dxdy} \tag{2.20}$$

where η is a fraction of energy from the incident beam that couples into the output fiber. $E_i(x,y)$ is the complex amplitude of the fiber mode to be coupled and $E_f(x,y)$ is the complex amplitude of the receiver fiber mode. The mathematical description of the beam clipping becomes visible in the non-infinite boundaries of the integral in the nominator of equation 2.20.

2.2.7 Gaussian Beam Decomposition

Gaussian beams maintain their shape as they propagate through an optical system. This characteristic makes them suitable to decompose an arbitrary optical field distribution into smaller Gauslets[9]. The amplitude and phase of the individual Gauslets can be propagated through an optical system using a ray-tracing approach. The coherent summation of the Gauslets gives the irradiance distribution at any point of the system including interference effects.

2.3 Hydro-fluoric Acid Vapour Phase Etching (HF VPE)

HF is a commonly used chemical in microfabrication. It has an ability to etch SiO_2 (silica) and certain metals at relatively high rates and has an excellent selectivity between silicon and SiO_2[10]. At room temperature HF is present in gaseous form. It is very soluble in water, which is the reason why it is most often present in an aqueous solution at different concentrations.

MEMS structures are often fabricated on silicon on insulator (SOI) wafers. They can be described as a sandwich structure of a thick silicon handle layer, a thin, intermediate SiO_2 layer and the silicon device layer with desired thickness. The MEMS devices are transferred from a mask into the device layer by means of a photolithographic step followed by an etching step (figure 2.9). The etching method is chosen so that the etching stops (or is considerably slowed down) at the buried SiO_2 layer. Some structures can be suspended by thin beams and anchored to larger area structures. By underetching the buried SiO_2 in HF acid the thinner structures can be released from the handle wafer.

The etching of SiO_2 in liquid carries a problem known as the sticking effect (figure 2.10). Sticking is often an irreversible and destructive phenomenon that occurs whenever liquids evaporate. The surface tension pulls movable structures down to the substrate or other fixed structures until they are in contact. When SiO_2 is etched in aqueous HF, rinsing in deionized water must follow to remove the contaminants. Unfortunately, water has a very high surface tension.

The use of a hydrofluoric acid vapour enables the removal of silicon dioxide in a vaporous environment rather than in an aqueous solution[11,12,13,14]. This is of particular interest since the wafer to be etched is never in direct contact with a liquid and sticking can be avoided. Additionally, extremely fragile structures can be released that would otherwise be destroyed by the surface tension of the liquid.

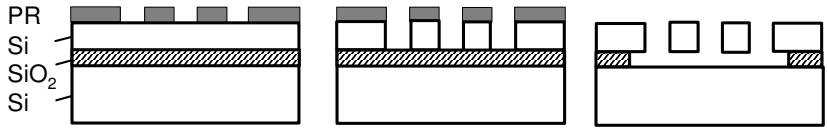

Figure 2.9: *Fabrication of MEMS on Silicon on Insulator (SOI) wafers: The desired structures are patterned in photoresist (PR) using a photolithographic process and transferred into the silicon. Finally, the movable parts are liberated by underetching the buried SiO_2 layer.*

The chemical reaction between HF and SiO_2 was first published by Offenberg *et al.*[15]. It is a two step reaction where first the SiO_2 surface is opened by formation of silanol groups by adsorbed H_2O. Subsequently silanol groups are attacked by the HF:

$$SiO_2 + 2H_2O \rightarrow Si(OH)_4$$

$$Si(OH)_4 + 4HF \rightarrow SiF_4 + 4H_2O$$

The above formula shows that water acts as initiator of the etching process as well as reactant. This fact suggests that the etch rate can be temperature controlled by maintaining the equilibrium of the amount of H_2O needed to initiate the process and the amount of reactant H_2O.

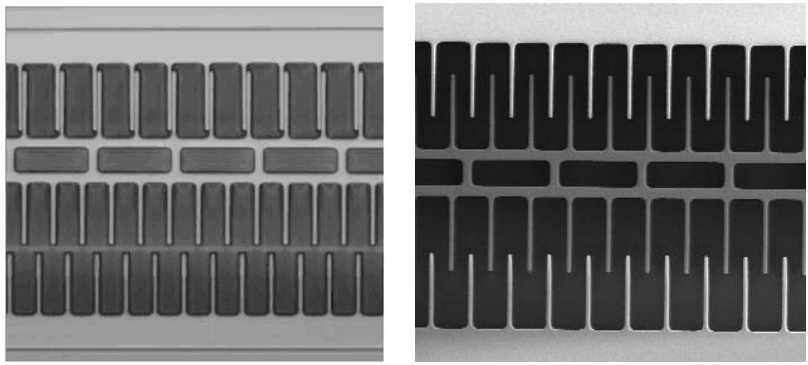

Figure. 2.10: *Left: A comb drive, freed in liquid HF acid, is sticking to the fixed structures due to the surface tension of the liquid. Right: Structure released with HF vapour. The sticking can be avoided.*

References:

[1] J. Tsaur, T. Kobayashi, M. Ichiki, R. Maeda, T. Suga, “An integrated Fabrication of Sol-Gel Derived PZT Thick Films and SOI wafers for 2D Optical Micromirror“, OMEMS 03, Hawaii.

[2] C. Ji, Y. Yee, J. Choi, S. Kim, J. Bu, ”Latchable Electromagnetic 2x2 Photonic Switch for low Power Operation”, OMEMS 03, Hawaii.

[3] H. Toshiyoshi, “Micro-Opto-Electro Mechanical Systems and their Applications”, Lecture, UCLA, USA.

[4] O. Manzardo, F. Scheadelin, Wilfried Noell, Nico de Rooij, H. P. Herzig, “Infrared MEMS-based lammelar grating spectrometer”, Proceedings of SPIE, vol. 5455, 2004 , pp .1 – 8.

[5] K. B. Lee, “Laterally driven Electrostatic Repulsive-force Microactuators using Asymmetric Field Distribution“, JMEMS, 2001.

[6] H. Siyuan, B. Mrad, “Development of a novel Translation Micromirror for Adaptive Optics“, SPIE, Vol. 5602, Bellingham.

[7] S. Yuan, A. Riza, “General formula for coupling-loss characterization of single-mode fiber collimators by use of gradient-index rod lenses”, Applied Optics, Vol. 38, No. 15, 1999.

[8] Saleh B, Teich M, “Foundametals of photonics”, Wiley, 1991.

[9] ASAP software documentation: asap_GBD_gausbeamdecomposition.pdf

[10] K. Williams, R. Muller, “Etch Rates for Micromachining Processing“, JMEMS, vol. 5, no. 4, Dec. 1996.

[11] J. Anguita, F. Briones, “HF/H2O vapor etching of SiO2 sacrificial layer for large-area surface micromachined membranes”, Sensors and Actuators, A 64 (1998), 247-251.

[12] M. Offenberg, B. Elsner, and F. Larmer, “Vapor HF Etching for sacrificial Oxide Removal in Surface Micromachining”, Electrochem

Society Fall Meeting, Vol. 94-2, Oct. 1994, Extended Abstract No. 671, pp. 1056-1057.

[13] C. R. Helms, B. E. Deal, “Mechanism of the HF/H2O vapor phase etching of SiO2”, J. Vac. Sci. Technol. A 10 (4), Jul/Aug 1992.

[14] A. J. Muscat, A. G. Thorsness, G. Montaño-Miranda, “Characterization of residues formed by anhydrous hydrogen fluoride etching of doped oxides”, J. Vac. Sci. Technol. A 19 (4), Jul/Aug 2001.

[15] M. Offenberg, B. Elsner, and F. Lärmer, “Vapour HF etching for sacrificial oxide removal in surface micromachining”, Extended Abstracts: Electrochem. Soc. Fall Meeting (Miami Beach) vol 94-2, pp 1056-7, 1994.

3 Concept

Sercalo's 2x2 optical cross connects are based on deep reactive ion etching (DRIE) of silicon-on-insulator (SOI) wafers[1]. A vertical mirror is actuated using an electrostatic comb-drive structure. Four optical fibers have to be assembled to the chip. The X-shaped arrangement allows the fibers to be brought very close together, which means that the optical path length that the light has to travel before being reinjected into the outgoing fiber is in the order of 100 µm. Therefore, the losses due to beam divergence are only in the order of 0.5 dB[2].

Larger port count optical switches can be created in two ways. First, they can be produced by cascading 2x2 elements. At every stage that is added, the coupling losses of the individual stages are added, which decreases the optical performance of the system. Another method to make larger port count optical cross connects is using a matrix of individually addressable mirrors, which will be explained in the next section.

A common inconvenience of optical MEMS is the assembly to external optical elements. The high alignment precision that is required for microoptical systems requires several precautions that need to be taken into account when designing the chip.

Passive alignment structures etched during the same step as the mirrors enable an economic assembly of optical fibers. A further improvement of this technique is a parallel assembly of fibers using commercially available fiber

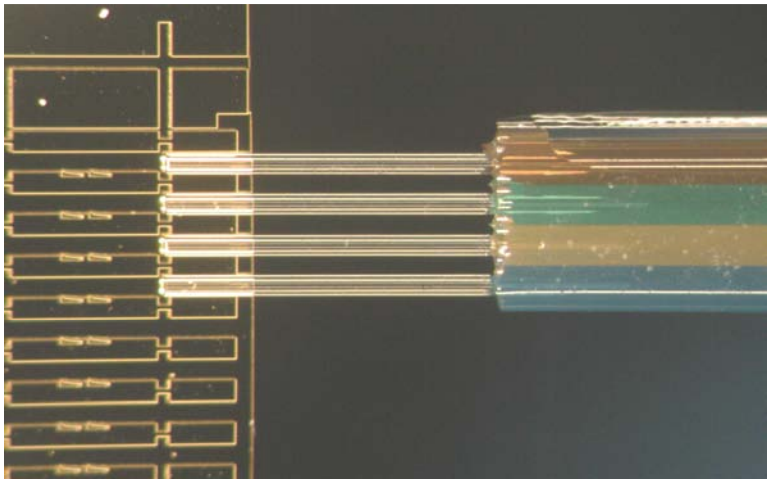

Figure 3.1: *Fiber ribbon containing four fibers with colour coded plastic jacket above silicon U-grooves for the fibers. The pitch between two neighbouring fibers is 250 µm.*

ribbons (figure 3.1). For the case of a single mode fiber used for telecommunication the pitch between neighbouring fibers measures 250 µm,

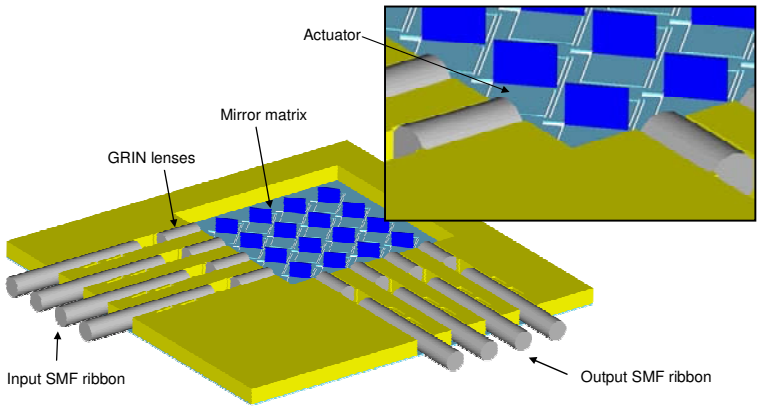

Figure 3.2: *Conceptual drawing of a 4x4 OXC: Fiber ribbons can be passively aligned to a 4x4 matrix of reflective mirrors, which have the same pitch as the fibers (250 µm).*

which defines the smallest reasonable pitch between microfabricated optical elements on a chip.

The goal of this project is straightforward: The fabrication of a dense 4x4 and 8x8 mirror matrix with a mirror pitch of 250 µm and actuators for individual addressing. The compact design of the switch allows the assembly of fiber ribbons instead of individual fibers. A conceptual drawing of a 4x4 OXC is shown in figure 3.2.

3.1 The MEMS Actuator

The layout of the required 4x4 mirror matrix is sketched in figure 3.3. The light of four input fibers is switched to any output fiber by setting the corresponding mirrors in the reflective state. Cylindrical GRIN lenses are used to collimate the light coming from the single mode fiber. The fiber ribbons and GRIN lenses are assembled into U-grooves etched during the same step as the mirrors. This enables passive alignment.

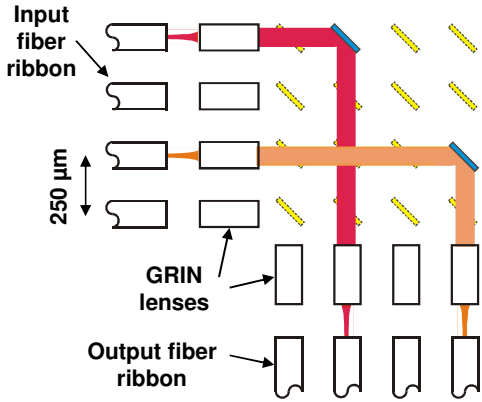

Figure 3.3: *Schematic layout of the 4x4 switch matrix. The mirrors have a pitch of 250 µm. The light of four input fibers is switched to any of the four output fibers by setting the corresponding mirrors in the reflective state.*

3.1.1 Optical Dimensioning

Before talking about the actuation principle I would like to focus on the dimensioning of the microoptical system and its influence on the mechanical design. The interaction of optical and mechanical properties has to be analysed before designing a device. An often underestimated effect is the divergence of small optical beams. The coupling length of an optical beam rises quadratic with the beam waist (see chapter 2.2.3). Since the Rayleigh Range is the double value of the distance where an initial beam waist ω_0 reaches a diameter of $\sqrt{2}\ \omega_0$, it will be taken as an indicator for an achievable coupling length. The Rayleigh Range in function of the beam waist is plotted in figure 3.4 and is compared to the coupling length requirements of the 8x8 OXC.

If we come back to the desired pitch of 250 µm it follows that for an 8x8 array the maximum coupling length would be 16 pitches or 4 mm. From figure 3.4 we can conclude that a minimal beam waist in the order of 30 µm

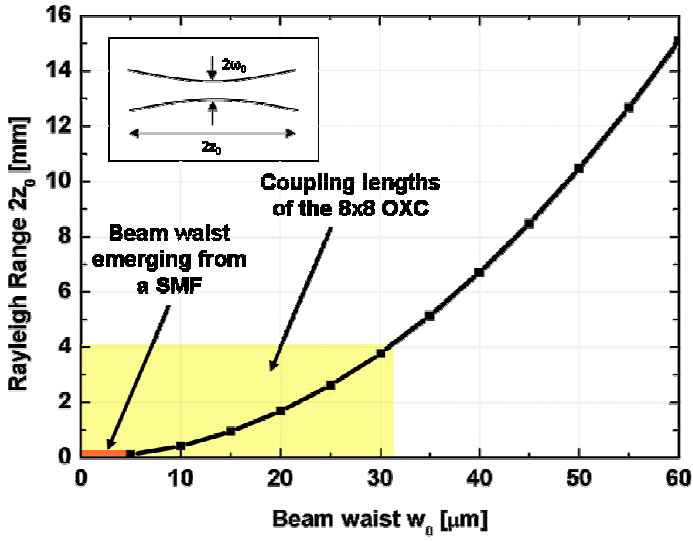

***Figure 3.4**: The Rayleigh Range can be taken as an indicator for an achievable coupling length for a given beam waist in the mirror matrix area. The Rayleigh Range of an optical beam emerging from a SMF is in the order of 100 µm. The maximum coupling length of the 8x8 OXC is 4 mm, which means that to couple light from input to output with low loss a beam waist larger than 30 µm should be chosen.*

will be required in the mirror matrix area.

Now the size of mirrors can be calculated. It follows from the geometry of a matrix switch that the incoming light beam can be reflected at almost any place on its axis of propagation. This means that we do not know the exact diameter and curvature of the beam that will be reflected. Therefore, a mirror size exceeding the size of the beams biggest extension should be designed. If we think again about the beam diameter at the Rayleigh Range a good estimation for the maximum beam waist is $\sqrt{2}\ \omega_0$. In order to reflect a light beam with a beam waist of 30 µm, a mirror height of 100 µm is appropriate ($2 \times \sqrt{2}\omega_0$). The mirrors are oriented at an angle of 45° to the optical beam. In order to have a projected length of 100 µm their length has to be $\sqrt{2} \times 100$ µm.

3.1.2 Electrostatic Actuator

By looking at the layout of the mirrors matrix we can eliminate the use of classical comb drive actuators. Their lateral size makes it impossible to integrate them between the individual mirrors. Additionally, a design that could move the mirror out of the optical plane, which is defined by the plane in which the light beams propagate, is preferred to a design where the mirrors are only shifted out of the optical path within the plane.
A very compact design can be found by looking at MEMS for display applications[3]. A platform, which is supported by torsion beams, is actuated by an electrode underneath. A silicon version of such a platform proved its reliability[4]. Whereas in both cases the platform itself acts as the reflective surface, our switch needs a vertical mirror, which is situated vertically on the top of the platform. The actuation principle remains the same and is shown in figure 3.5. In the initial state a voltage is applied to all the electrodes and the platforms are grounded. The actuators are pulled down and do not affect the light beams. Once the voltage on the addressed electrode is switched off, the corresponding actuator bends up due to the restoring force of the torsion beams. The light beam is switched to the corresponding output fiber.

The size of the platform should be as big as possible to optimise the electrostatic force actuating the device. The length should match the vertical mirror and was fixed to 140 µm. The width is limited by the pitch of the mirrors. After designing a supporting frame a maximum width of 280 µm remained.

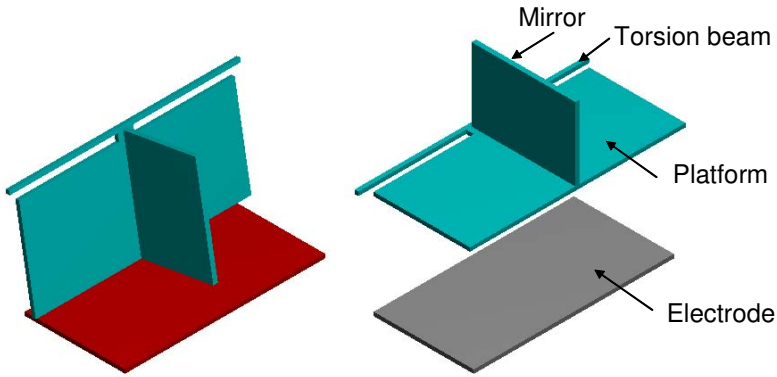

Figure 3.5: *Platform with vertical mirror in the actuated (left) and non actuated (right) state. A light beam is only reflected if the mirror is in the non-actuated state.*

The complete switch is composed of a matrix of such actuators (figure 3.6). The design of the electrodes comprises the wiring to a surrounding

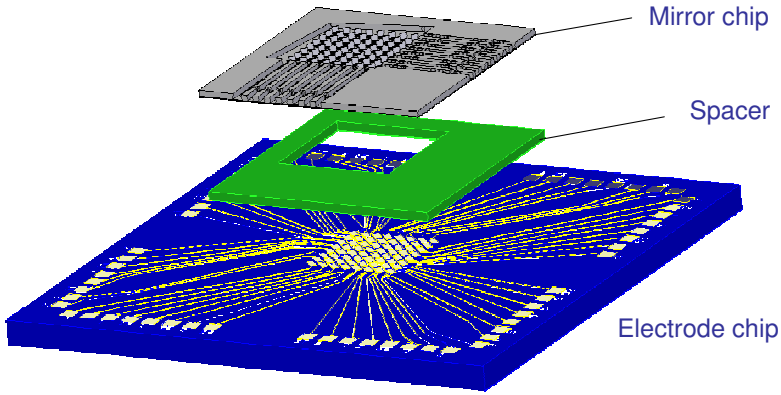

Figure 3.6: *Array of actuators and electrodes: A spacer ensures the correct spacing between the two parts.*

bondpad area, which allows the bonding to the driving electronics. A spacer ensures the correct spacing between mirror and electrode array.

3.1.4 Electrostatic Simulation

The goal of this subchapter is the estimation of the available actuation forces and the determination of the dimensions of the torsion beams. The out-of-plane actuation of the platform requires an actuation electrode under the platform spaced by a spacer. The height of the spacer is given by the length of the platform (140 µm). To avoid touching or sticking of the two components due to bending of the torsion beams an additional height of 10 to 20 µm was added. To move the mirror out of the optical path a voltage is applied to the electrode while the platform is at ground potential.

The high distance between the two electrodes results in a small electrostatic force. The restoring force of the torsion beam can be calculated explicitly[5]. For small angles, a parallel plate capacitor approximation can be used to calculate the force of the actuator for a given voltage. The result of this calculation was that at an actuation voltage of 200 V the diameter of the torsion beams would have to be less than 1 µm.

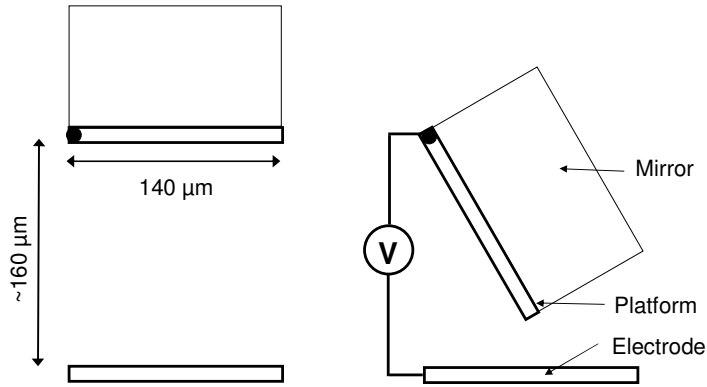

Figure 3.7: *Cross section of the actuator and actuation principle. If a voltage is applied between platform and electrode the platform moves out of the optical plane.*

Of course, the parallel plate approximation is not exact for this kind of actuator but it is simple and gives a first estimate for the actuation voltage. To obtain a better understanding of the device different FEM simulations and the energy method described in chapter 2.1.1 were performed. The most important task to solve was the influence of the torsion beam cross section on the actuation voltage.

3.1.4.1 Coventor Ware: Finite Element Method

All coupled electromechanical FEM simulations were carried out with CoventorWare. For simplicity, square beam cross sections were simulated. The tilt angle of the platform in function of the voltage is plotted in figure 3.8. To show the strong dependency of the beam cross section we varied its height from 0.25 to 2 µm keeping the width constant at 1 µm.

From figure 3.8 it can be seen that a doubling of the beam height causes approximately twice the actuation voltage. At higher tilt angles than plotted

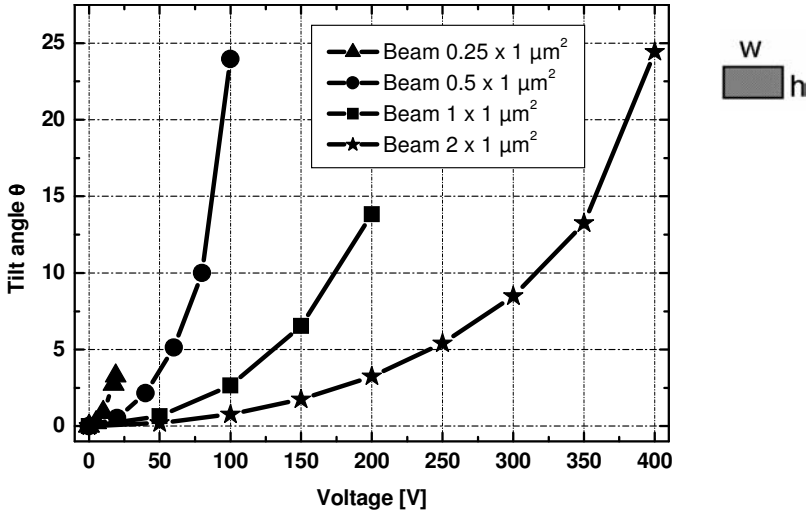

Figure 3.8: *Comparison of the tilt angle in function of the applied voltage for different beam cross sections. A doubling of the beam height causes approximately a doubled actuation voltage.*

we observed a pull-in of the platform. However, the platform and electrode never touched since the chosen height of the spacer was 20 µm higher than the length of the platform.

The corresponding simulated resonance frequencies of the first mode are shown in table 3.1. It has to be noted that these values were calculated for a solid platform with the height of the beams and without any mirror and do not reflect exactly the microfabricated device.

Table 3.1: *Simulated resonance frequencies of the first mode; the beam width w of 1 µm and the length of 150 µm are constant. The resonance frequency increases with the beam height due to the increased torsion spring constant.*

Beam height h [µm]	Resonance frequency [kHz]
0.25	0.79
0.5	1.47
1	2.41
2	3.19

3.1.4.2 Energy Method

The FEM simulation showed that the principal motion of the platform is the tilt motion around the axis of the supporting torsion beams. The sagging of the platform was in the order of 1 µm at tilt angles close to 90°. The comparison of the mechanical energies that are stored in the torsion and sagging mode of the torsion beams show that only a negligible amount of energy is stored in the sagging mode. Therefore, it is possible to simulate the device using the energy method and to neglect the sagging of the platform.

ANSYS and Coventor were used to create two electrostatic models of the actuator. The major difference between the two softwares is that in ANSYS we computed the total electrostatic energy that is stored in the system whereas Coventor computes the capacity. Another difference is that in ANSYS the two electrodes were modelled using a 2D approach whereas in Coventor a 3D model was created. Therefore, it was possible to create a

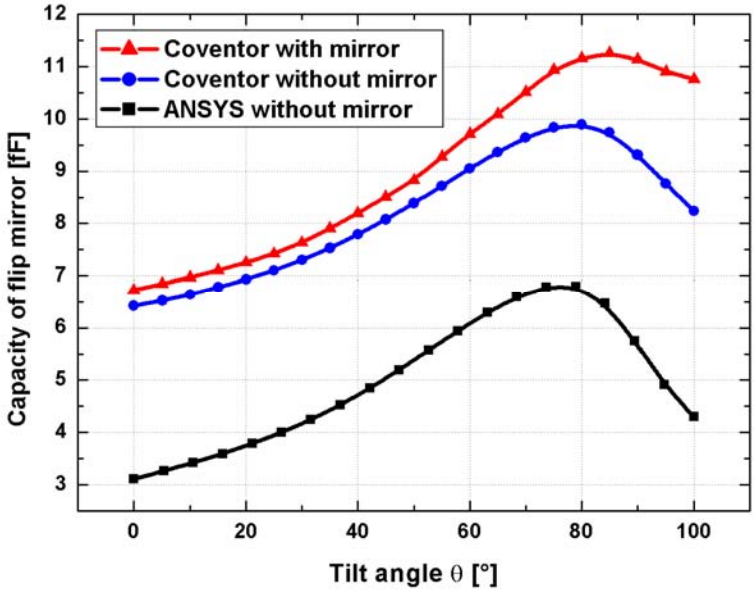

Figure 3.9: *Simulated absolute value of the capacity for different tilt angles for three different models. A 2D model was used in ANSYS whereas a 3D model with and without mirror was simulated with Coventor.*

Coventor model including the vertical mirror which was not the case for the 2D model.

The absolute value of the simulated capacity for different tilt angles is shown in figure 3.9. The influence of the vertical mirror can be seen clearly. The initial value of the capacity is higher with the mirror and as the tilt angle increases the distance between mirror and electrode decreases causing an increase in capacity. At first sight it seems that the ANSYS results differ strongly from the results obtained by Coventor. However, it has to be reminded that the force acting on the actuator is proportional to the first derivate of the capacity. The derivate of the capacity is shown in figure 3.10. Here, the ANSYS and the Coventor model without mirror show nearly equal results. Only the model with the mirror shows a higher force at tilt angles over 45°, which again is explained by the additional force originating by the presence of the mirror.

The reason behind the discrepancy in the absolute value of the capacity must be in the mathematical models of the two softwares. The electrostatic energy is distributed over an infinite volume. The ANSYS model covers only

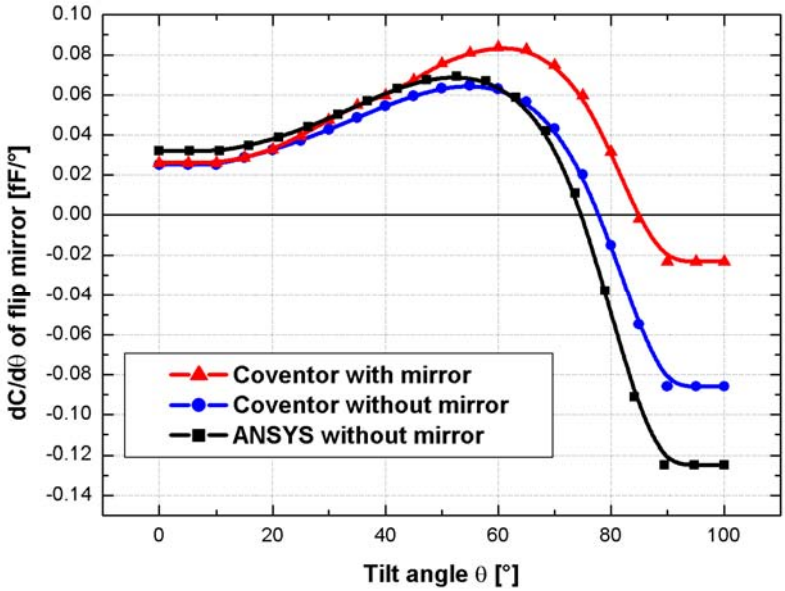

Figure 3.10: *The electrostatic force acting on the actuator is proportional to the derivate of the capacity. The ANSYS and Coventor results show nearly equal results. The additional force acting on the mirror causes a higher force at tilt angles greater than 45°.*

a finite volume. Coventor creates a finite model surrounded by infinite boundary elements but it is not clear how it calculates the capacity. The initial capacity of the actuator can be calculated by the parallel plate approximation, which gives a value of 2.15 pF being closer to the ANSYS simulation.

These results shown in figure 3.10 were exported to Matlab where the mechanical energy stored in the torsion beams was subtracted. Figure 3.11 shows a V-θ diagram at the equality of mechanical and electrostatic torque of the actuator for a square beam cross section of 1x1 μm^2. As anticipated from figure 3.10, the results obtained by the different simulation softwares agree very well. The presence of the mirror decreases the actuation voltage by only 20 V. The maximum tilt angle increases from about 75° for the platform to over 80° for the platform including the mirror. In comparison to the pure FEM simulation shown in figure 3.8 the values obtained by the energy method agree very well for the tilt angles that were calculated by the FEM. However, the energy method showed that the platform does not pull-in, as

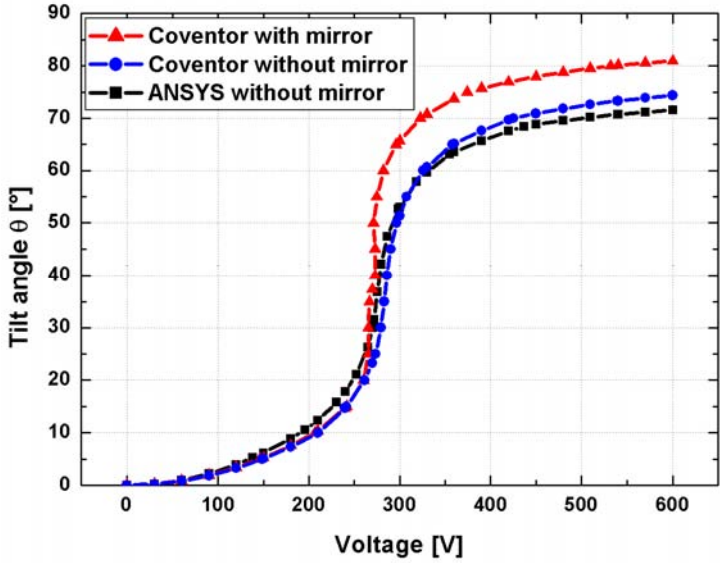

Figure 3.11: *V-θ diagram at equality of mechanical and electrostatic torque of the actuator for a square beam cross section of 1x1 µm² calculated by the energy method. The results obtained by ANSYS and Coventor, as well as the pure FEM simulation, agree very well.*

seen using a FEM analysis. The high slope of the curve between 20° and 50° caused the FEM algorithm to fail.

The main conclusion that can be drawn from this chapter is that the cross section of the torsion beams will have to be in the order of 1 µm² to drive the mirrors at reasonable voltages around 300 V.

Structures with such small dimensions are difficult to fabricate. Different types of independent fabrication tolerances make it difficult to predict the exact size of the microfabricated structure. The main sources of these tolerances originate from the mask, the lithography, the development of the photoresist and the etching method as well the etching itself. Typically, the structures on a mask are defined with a tolerance of ± 0.1 µm (see figure 3.12). The lithography and development tolerances lie in the same order of magnitude. Tolerances from the etching method vary between 0 and several micrometers, however, values in the micrometer range are mostly observed during wet etching. Modern plasma etching machines achieve an underetching in the order of 0.1 µm.

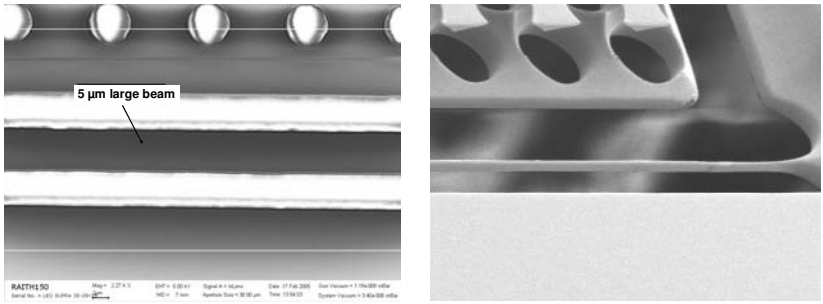

Figure 3.12: *Left: SEM micrograph of the chromium structure on the photolithographic mask. The designed beam width was 5 µm. A clear thickness variation of ±100 nm is visible. Right: Microfabricated torsion beam after the beam thinning. The beam thickness is in the order of 1 µm. The thickness variation of the mask was transferred to the beam.*

A common way to fabricate small silicon structures is to design a slightly larger structure width and to tune the width by a timed thermal oxidation of silicon followed by a removal of the SiO_2[6]. This method will be further explained in the next chapter.

3.1.5 Process Flow

The search for an appropriate process was difficult. Etching thin, vertical and 100 µm high mirrors is already complicated in and of itself. If the verticality of the structures is not controlled to a fraction of a degree thin structures are undercut and are lost during the etching process (figure 3.13). A process allowing to etch mirrors supported on a thin platform and very fragile torsion beams had to be found. A delay mask process[7] where the beams and platforms were etched from the front-side was not suitable because of the long second etching step. The only way to fabricate structures with high resolution on the top and bottom side of the device was using a double side process and taking wafers with a thickness of the device itself. The SCREAM process[8] that was developed to fabricate thin, suspended structures in bulk silicon using a single lithography step was found to be a

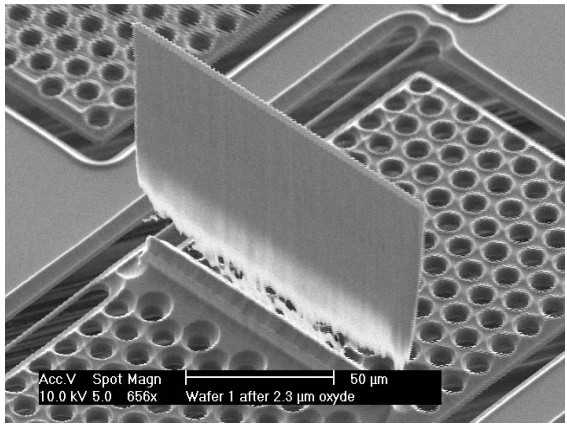

Figure 3.13: *Thin mirror, underetched due to a slightly negative etching angle.*

good inspiration. The idea to combine directional etching, passivation, directional etching of the passivation and isotropic underetching of a thin beam was adapted to our needs.

The fabrication process is shown in figure 3.14. It starts with a thin silicon wafer. The thickness measures 120 µm, which is the height of the actuator (mirror and platform).

1) A thick (1 µm) thermal SiO_2 is grown on the wafer. Photoresist is spun on the backside and patterned using a photolithographic process. This step defines the initial beam width and the platform.
2) The SiO_2 is dry-etched using reactive ion etching (RIE). This pattern is transferred to the silicon using deep reactive ion etching (DRIE). 7 µm deep trenches are etched into the wafer. After stripping the photoresist and cleaning, a thin (0.3 µm) thermal SiO_2 is grown. This step does not increase the thickness of the thick SiO_2 by the same amount as on the bare silicon in the trenches.
3) The SiO_2 is dry etched in a directional (anisotropic) plasma etch. This allows the removal of the floor SiO_2 in the trenches while leaving some SiO_2 on the sidewalls and the area that was covered with thick SiO_2 protecting these surfaces during the next step. A dry, isotropic silicon etch releases the beams due to the undercut. This technique enables the fabrication of beams of the same dimensions over the whole wafer.
4) After cleaning, another thin (0.3 µm) SiO_2 is grown. It coats the whole beam, which will protect it during the following front side processes. The

thin and fragile silicon wafer is anodic bonded to a 500 µm thick Pyrex wafer. The patterned side is facing the Pyrex wafer. A photoresist layer is spun and patterned on the front side of the silicon wafer to form the mirrors. The SiO_2 is dry etched using RIE.

5) The mirrors are etched using DRIE. The etching is stopped when the SiO_2 protecting the beams becomes visible. The Pyrex wafer and the SiO_2 are removed by concentrated HF. The beams are thinned to the desired thickness reiterating the thermal oxidation and HF VPE of silicon. VPE is preferred to wet etching because the surface tension of liquid HF and the following rinsing in DI water would break the fragile torsion beams. A 50 nm thick layer of gold is sputtered on the mirrors to ensure a good reflectivity in the infrared band. Finally, the actuator chip is assembled to an electrode chip, which consists of a Pyrex substrate as well as etched metal electrodes and an isolating spacer.

Dicing is a big problem for Optical MEMS. The harsh water jet cooling the dicing blade in common wafer dicing machines can break the fragile structures once they are released. Additionally, the reflective surfaces need to be protected from the dust generated by the dicing process. One method is covering the entire wafer with photoresist, dicing the wafer and removing the photoresist from the chips after the dicing. However, this process brings the

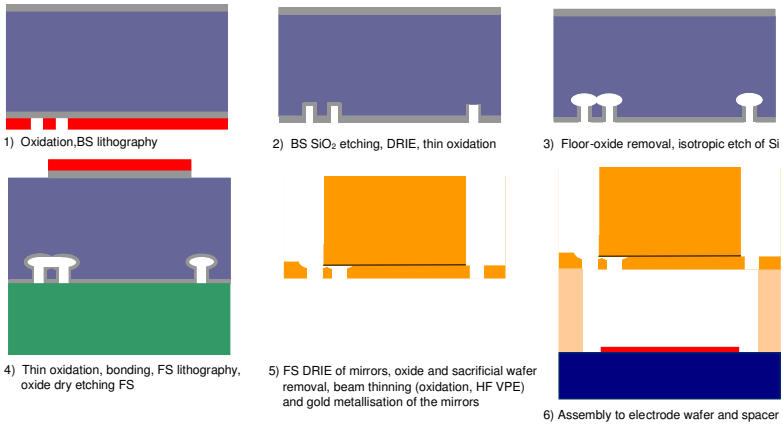

Figure 3.14: *Process flow: Double sided etching of a thin silicon wafer enables the fabrication of high resolution structures on both sides of the wafer. The thin torsion beams are fabricated on the back-side (BS) of the wafer. The vertical mirrors are etched on the front-side (FS). Finally, the fragile silicon chip is assembled to the spacer and the electrode chip.*

released structures in contact with a liquid which is not desirable. A method for dicing free release was proposed by Overstolz et al.[9]. This method is only applicable for SOI wafers if both sides are patterned. In our case we decided to attach the chips with tiny beams to a silicon grid. These beams are etched during the fabrication of the device and can be easily broken manually once the fabrication is done. Using this method it also becomes possible to break out individual chips during their fabrication, which offers a better process control without the need of inspecting the whole wafer.

3.2 The Micro-GRIN Lenses

The relatively large coupling length in an NxN switch matrix requires a collimating lens system in order to broaden the beam waist coming out of the single mode fibers. Cylindrical GRIN lenses have a big advantage in that they can easily be aligned to the cylindrical shape of optical fibers. However, GRIN lenses with a diameter of 125 µm are not commercially available. Such lenses could be easily integrated and aligned to single mode fibers using a U-groove that is defined on one mask. The schematic of such a collimation system is shown in figure 3.15.

A new and inexpensive approach to fabricate micro GRIN lenses with a diameter of 125 µm is based on the dicing of selected multimode fibers with a GRIN core distribution, which will be presented in the next chapter[10]. The focal distance of the GRIN lens is adjusted by its length. Therefore, the coupling losses in function of the GRIN lens length and coupling length were studied and are presented hereafter.

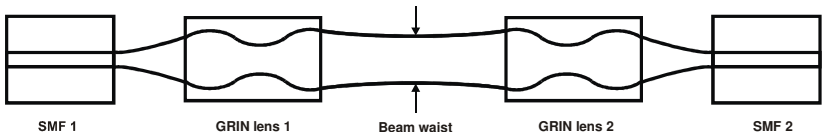

Figure 3.15: *Schematic of the collimating setup: A light beam emerges from the SMF 1 and is collimated by GRIN lens 1. GRIN lens 2 refocuses the beam into SMF 2.*

3.2.1 Optical Simulations

The coupling efficiency of the collimating system outlined in figure 3.15 is calculated using two different approaches. The first approach is the calculation using *ABCD* matrixes described in chapter 2.2. The second method is Gaussian Beamlet simulation using the commercial software FRED from Photon Engineering. The simulations show the influence on the coupling efficiency of the following parameters:

- Length of the GRIN rods
- Tolerance of the GRIN rod length
- Distance between SMF and GRIN lens
- Achievable coupling length for a given maximal coupling loss

For all simulations a symmetrical setup as depicted in figure 3.15 was studied. The free space region was assumed to be a medium matching approximately the refractive index of the GRIN fiber.

Fabrication tolerances of the fiber manufacturer can change slightly. To avoid having to repeat the simulations for different fibers, we decided to

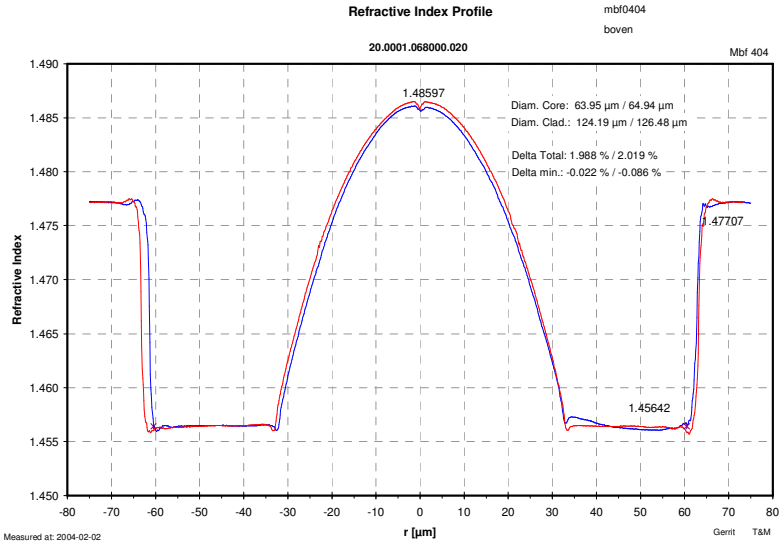

Figure 3.16: *Measured refractive index distribution of the selected MM-fiber.*

purchase a larger quantity of the selected GRIN fiber, thus ensuring a constant quality of the diced GRIN lenses.

The refractive index distribution of the fiber is shown in figure 3.16. The GRIN fiber core had a diameter of 64 µm and a NA of 0.269, which results in a parabolic factor $\alpha = 0.006$ mm^{-1} ($n^2 = n_0^2 [1-\alpha^2 r^2]$). All important parameters for the fiber are summarized in table 3.2.

Table 3.2: *Summarized parameters of the selected MM fiber.*

Core diameter [µm]	Numerical aperture NA (data sheet)	n_0	Parabolic constant α [mm^{-1}] (fitted value)	Pitch (2π/α) [µm]
64	0.269	1.486	0.006	1047

3.2.2 Coupling Efficiency Using the Paraxial Approximation

The ABCD law is a straightforward method to calculate the coupling efficiency for Gaussian beams. However, it does not take into account the losses originating from diffraction and its paraxial nature makes it unsuitable

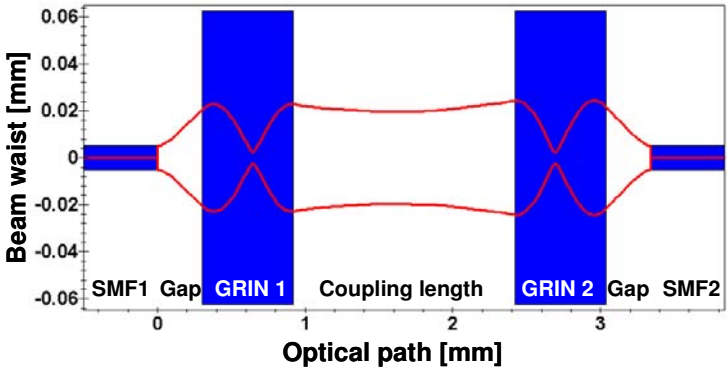

Figure 3.17: *Calculation of the beam waist in a collimator setup. The light beam emerging the SMF1 diverges and is collimated by GRIN lens 1.*

for calculating angular misalignment losses.

Figure 3.17 shows the calculated propagation of the beam waist in the collimator setup. The light beam exiting SMF1 diverges and is collimated by GRIN lens 1. The distance between SMF1 and GRIN1 determines the size of the beam waist in the lenses as well as in the free space region where other optical elements can be placed. Care has to be taken that the beam waist does not exceed the size of the lenses. With a gap distance of 400 µm the beam waist already extends to a beam diameter of 60 µm in GRIN1.

Figure 3.18 shows four calculations for different gap lengths between SMF and GRIN lens. Each graph represents the coupling losses of the whole system in function of GRIN- and coupling length. To reduce Fresnel reflection and diffraction losses the setup is assumed to be immersed into index matching fluid with a refractive index of 1.45 closely matching the refractive index of the lens. The centre of the GRIN lens has a refractive index $n_0 = 1.48$. The utilized wavelength λ is 1.55 µm.

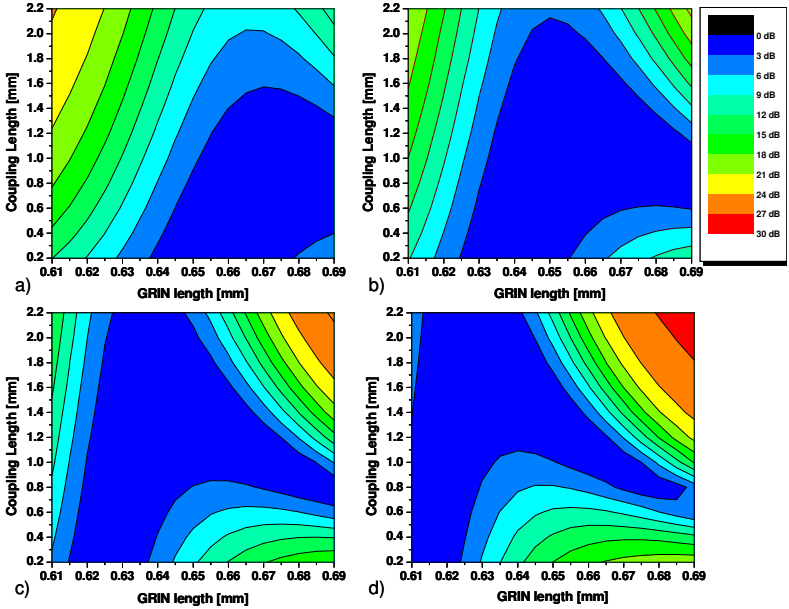

Figure 3.18: *Coupling loss as function of GRIN lens length and coupling distance: a) 200 µm, b) 250 µm, c) 300 µm, d) 350 µm. A larger gap between SM fiber and GRIN lens increases the coupling length and shorter GRIN lenses need to be taken.*

Several conclusions can be drawn from these graphs. First, the length tolerances for a collimating lens are rather tight. A length variation of 10 µm increases the losses by several dB. It is apparent that the wider the gap between the GRIN lens and the SMF the larger the region of acceptable collimation. This is explained by an overall broadening of the propagating beam. However, the mathematical model does not take into account the losses that occur when the beam exceeds the core of the GRIN lens. Therefore, it is only valid for relatively small beam waists that are confined within the core of the lens.

The comparison of the performance of collimator systems having different gap sizes between the SMF and the GRIN lens is shown in figure 3.19. For a fixed coupling distance the optical losses can be minimized by choosing the right lens length. However, in some cases a small loss over a large coupling length is required[11]. A gap size of 350 µm in conjunction with a 610 µm GRIN lens delivers the best results over 2.3 mm keeping the losses relatively constant and lower than 3 dB.

A collimation system based on GRIN fibers with a core of 125 µm yields four times the coupling length. According to the simulations we should be able to fabricate lenses with a coupling length of 10 mm having overall losses

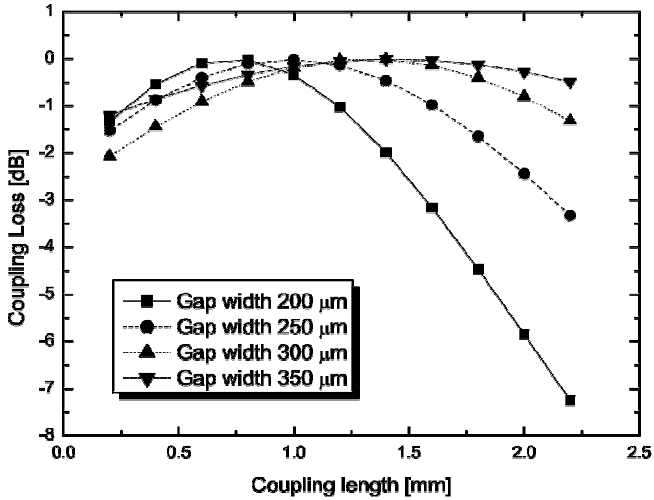

Figure 3.19: *Simulated effect of the gap width on the coupling loss. A large gap leads to a smaller overall loss. However, a small gap can be preferred for a fixed, short coupling length.*

less than 3dB. After consultation of the fiber manufacturer we decided to study GRIN lenses with a core diameter of 110 µm. A custom made fiber would allow us to obtain a fiber with an optimal refractive index distribution α. Since α is coupled to the NA, a series of simulations with variable NA was performed and is shown in figure 3.20. The NA has to be larger than the NA of the SMF (being approximately NA ≈ $\theta_0 = \lambda/\pi\omega_0 \approx 0.1$). The whole setup was again immersed in index matching fluid. During the first simulations the gap between SMF and GRIN lens was kept constant at 450 µm (figure 3.20 a), b), c)). The maximum beam diameter in GRIN 1 is 79 µm. The GRIN lens length tolerance, which is represented by the width of the blue region, decreases with the NA. The achievable coupling length at a given coupling loss also decreases if the gap is kept constant.
However, at larger NA the beam in GRIN 1 is focalized stronger which results in a smaller maximum beam waist. To be able to compare the

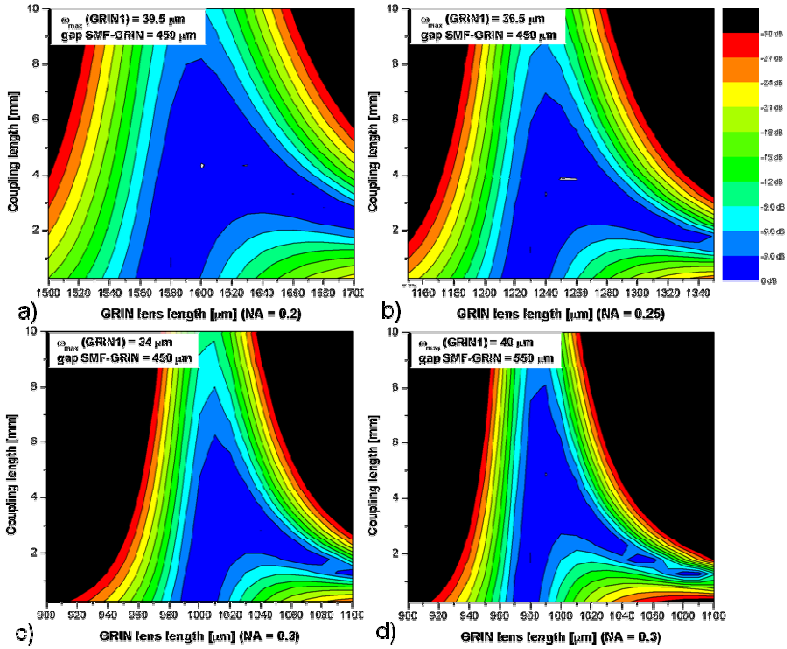

Figure 3.20: *Coupling loss as function of GRIN lens length and coupling distance for GRIN fiber with core diameter of 110 µm: a) NA = 0.2, b) NA = 0.25, c) NA = 0.3 µm, d) NA = 0.3 with corrected gap SMF-GRIN. Coupling length of 8 mm with losses < 3 dB are achievable. A smaller NA yields a larger length tolerance which facilitates the lens fabrication.*

performance of the GRIN lenses with different NA the gap between SMF and GRIN lens should be adjusted in order to have the same maximum beam diameter in GRIN 1. Figure 3.20 d) shows such a simulation for a NA of 0.3 and a beam diameter of 80 µm resulting by a gap length of 550 µm. If it is compared to figure 3.20 a) it is visible that the coupling length is practically equal but the lens length tolerance of the lens with larger NA is smaller.

3.2.3 Gaussian Beamlet Simulation

As mentioned in the previous chapter, the paraxial calculation of optical beams does not take into account the losses originating from diffraction at apertures and beam clipping. The software FRED from Photon Engineering combines ray tracing and the theory of Gaussian beamlets in one algorithm.

To validate the results shown previously the same setup as simulated in figure 3.20 a) was simulated with FRED. The results are shown in figure 3.21. Instead of an increased coupling loss due to a contribution of the diffraction effects the simulated losses are smaller than predicted by the paraxial approximation. This is caused by the sampling of the source beam, which becomes a trade off between the number of sampling points of the source and the divergence angle of the individual Beamlets. In the FRED result a looping of the low loss area for short lens lengths and coupling distances larger than 4 mm is visible. This effect is due to the beam clipping

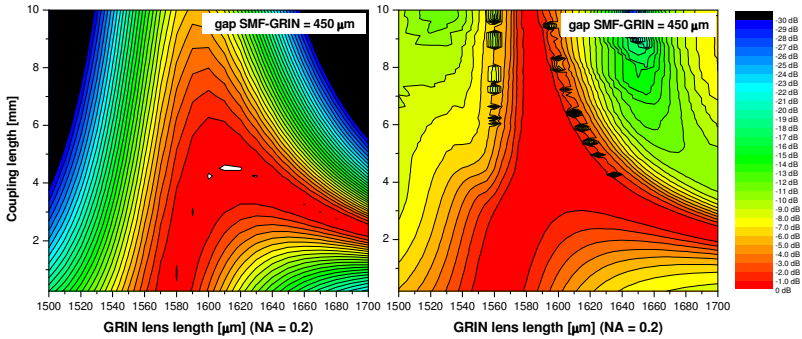

Figure 3.21: *Comparison between the coupling losses of the GRIN collimator system using ABCD matrices (left) and the software FRED (right). The FRED simulation yields considerably lower losses, which is probably due to the sampling of the light source.*

as a result of the large optical beams that are not coupled completely into the second GRIN lens. The simulated optimal GRIN lens length for this setup was found to be around 1590 µm for both simulation methods.

Even though the FRED results seem to predict lower losses than expected, the fact that the shape of the obtained curve agrees very well with the paraxial calculation indicates that FRED can be used to simulate the performance of microoptical elements in the discussed size in a qualitative way. The use of FRED is especially recommended for off axis simulations which can not be calculated by the paraxial method.

3.3 The Optical Cross Connect (OXC)

The difficulty of creating a microsystem lies rarely in the single component that is integrated on the chip. Single components are often very well understood but when they are built together the interaction between optics, mechanics and electrostatics raises new and unexpected phenomena.

Even though a design was chosen that allows the parallel assembly of fiber ribbons the assembly of the optical cross connect is an important task. Due to the small space available for the actuators, a stacking of different components becomes necessary.

3.3.1 The MEMS Part

The MEMS part of the optical cross connect consists of a stack of three chips: The electrode chip, the spacer and the silicon actuator (figure 3.22). The fabrication sequence of the silicon actuator was presented in chapter 3.1.5. The spacers are fabricated using thin Pyrex wafers that are etched to the desired shape using a poly-silicon mask and HF wet etching. The advantage of Pyrex is that it is a dielectric material, which electrically isolates the actuator chip from the electrode chip. A very important feature of Pyrex is that it can be bonded to silicon using the anodic bonding process[12]. By heating (around 360°C) and applying a voltage (several 100 V) between Pyrex and silicon an adhesiveless, chemical bond is created at the interface of the two materials. The latter is very important because the thinness of the silicon actuator prohibits any gluing that generates mechanical stress.

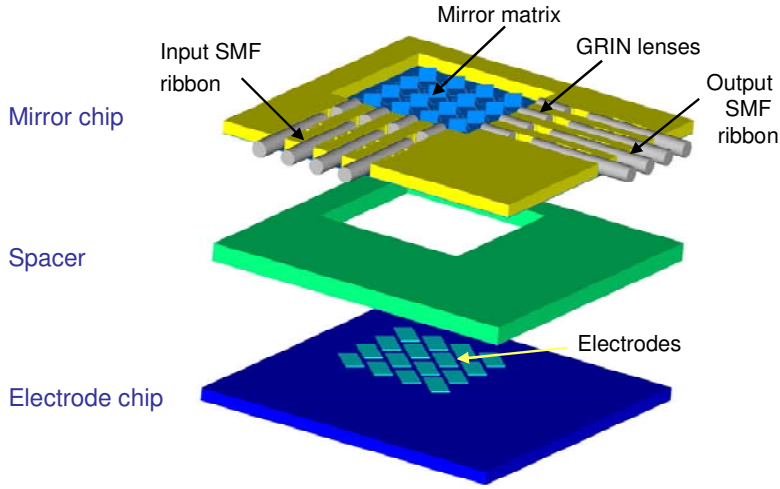

Figure 3.22: *Stack of electrode chip, spacer and mirror chip. The silicon actuator is anodic bonded to the Pyrex spacer, which is then glued on the electrode chip.*

The electrode chip consists of a patterned aluminium structure on a Pyrex wafer. Its function is the selective actuation of single mirrors and the electrical connection to the exterior (electronic) world. The gained rigidity of the Pyrex-silicon stack allows the use of epoxy-glue for the assembly to the electrode chip. The alignment of the two parts can be carried out under an optical microscope using a xyz and θ stage. The alignment accuracy should be in the order of 10 µm.

3.3.2 The Optical Assembly

The tininess of the GRIN lenses demands a micro-positioning tool that is able to handle such small cylinders. Sixteen individual GRIN lenses and two fiber ribbons containing eight fibers each have to be assembled to the MEMS chip.

3.3.3 The Assembly to the PCB and the Sealing

The microchip is assembled to a printed circuit board (PCB), which contains the macroscopic electrical connections to the driving electronics. The connections between electrode chip and PCB are made by wire bonding. To decrease losses due to Fresnel reflection and beam divergence the whole chip is filled with index matching fluid having a similar refractive index as the optical fibers ($n \approx 1.46$). A surrounding aluminium frame is glued on the PCB. After injecting the index matching fluid the chip is capped with a piece of glass, which is glued on the frame. A schematic of the chip assembly is shown in figure 3.23.

3.3.4 The Driving Electronics

The driving voltage of 300 to 500 V requires a voltage amplifier that generates these high voltages from a low voltage source. The electrostatic actuators do not need a high driving current. An electrical current flows when the small capacitance of the actuator is charged or discharged. The capacitance of our actuators is in the order of several fF. This value is negligible compared to the drain-source capacity of a switching transistor that is needed to "turn the actuation voltage on", which is in the order of pF.

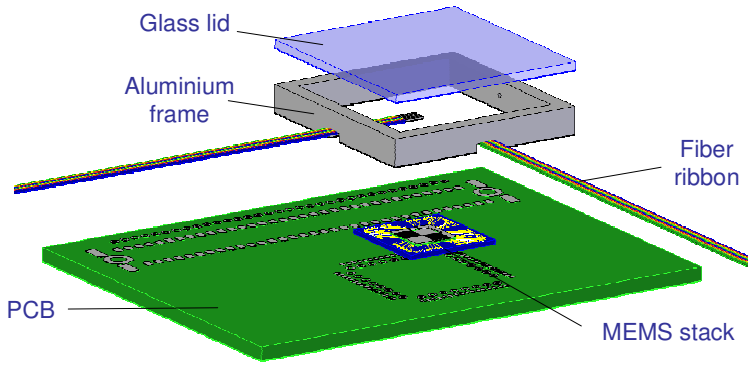

Figure 3.23: *Exploded view of the OXC including PCB, optical fibers, MEMS part, aluminium frame and glass lid.*

Step-up voltage converters are a very convenient way to convert low DC voltage into high voltage. Their working principle is the use of voltage peaks that are generated when the voltage is switched at high speed over an inductance[13].

The converter is based on a Maxim 770 CSA, which uses an external high voltage MOSFET transistor for the step-up conversion of the input voltage. The lower part of figure 3.24 shows the electrical schematic of the DC-DC converter block. The second building block of the electronic driver is the high voltage switches, which translate the logic input levels into the appropriate voltage to be applied on the electrostatic actuator. For our application we have chosen a N-MOS logic circuit. Its design is simple and allows us to tune the switching voltage with a second resistor for each mirror individually (figure 3.24 top). Nevertheless, for every N-MOS transistor that is set "high" (i.e. electrode on ground potential) a small current is drawn from the supply resulting in non negligible power consumption at 400 V. By Ohm's law, the

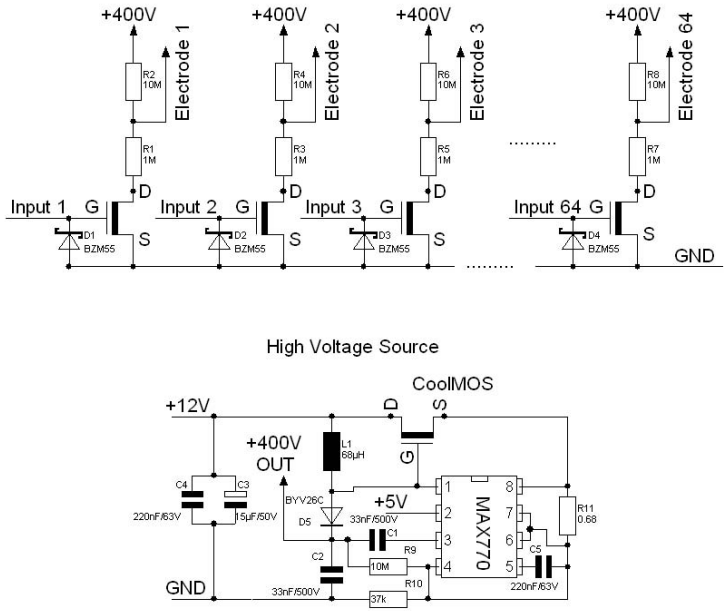

Figure 3.24: *High voltage generation (bottom) and switching of the individual electrode voltages (top) for the 8x8 OXC. A step-up circuit based on a MAX770 circuit converts a low DC voltage into 400 V DC or more.*

power flowing through a resistance is given by $P = U^2/R$, which results in 15 mW per channel if an 11 MΩ load is used. Typically, eight mirrors are in the switching state. Therefore, the theoretic power consumption of a complete 8x8 OXC is 120 mW. This value does not include the efficiency of the step-up circuit, which can be low if a high output voltage is desired. It has to be noted that the switching power (power that is needed to load the Drain-Source capacity of the transistors) is negligible.

The power consumption can be reduced by raising the value of the load resistor. However, this decreases the switching speed of the actuator since the RC value of the resistor and the drain-source capacity rises. A typical drain-source capacity for a SMD high voltage transistor is 10 pF. If it is loaded through a 100 MΩ resistance, it will take about 1 ms to actuate the mirror at a power of 0.8 mW per mirror for an actuation frequency of 500 Hz.

References:

[1] C. Marxer, C. Thio, M. Grétillat, N. F. de Rooij, R. Bättig, O. Anthamatten, B. Valk, P. Vogel, "Veritcal mirrors fabricated by deep reactive ion etching for fiber-optic switching applications", JMEMS Vol. 6, No. 3, 1997, pp. 277-285.

[2] Sercalo, "Latching Fiber Optic MEMS Switch", datasheet, http://www.sercalo.com

[3] Vuilleumier, R.; Perret, A.-E.; Porret, F.; Weiss, P., "Novel electromechanical microshutter display device", Fourth Display Research Conference, Eurodisplay '84 Proceedings, pp. 41-4 , 1984.

[4] Toshiyoshi H, Fujita H., "Electrostatic micro torsion mirrors for an optical switch matrix", Journal of Microelectromechanical Systems, vol.5, no.4, Dec. 1996, pp.231-7.

[5] Warren C. Young, "Roark's Formulas for Stress & Strain", Mc Graw Hill, 1989, New York.

[6] M. Zickar, Wilfried Noell, Cornel Marxer, Nico de Rooij, "4X4 & 8X8 Optical Cross Connect for Optical Fiber Networks", Proceedings of SPIE, vol. 5455, 2004 , pp .212 – 219.

[7] M. Mita, H. Toshiyoshi, T. Oba, Y. Mita, H. Fujita, "Multi-height HARMS by Planar Photolithography of Initial Surface", In Proceedings of High Aspect Ratio Micro Structure Technology (HARMST '99), pp. 28-29, June 13-15, Chiba, Japan.

[8] Kevin A. Shaw, Z. Lisa Zhang, Noel C. MacDonald, "SCREAM I: a single mask, single-crystal silicon, reactive ion etching process for microelectromechanical structures", Sensors and Actuators A, 40, 1994, pp. 63-70.

[9] T. Overstolz, P. A. Clerc, W. Noell, M. Zickar, N. F. de Rooij, "A clean Wafer-scale Chip-release Process without Dicing based on Vapor Phase Etching", MEMS 2004, Maastricht NL, pp. 717-20.

[10] International Patent Application: “Optical Coupling Element and Method of Manufacturing the Optical Coupling Element“, PCT/IB2004/001611.

[11] M. Zickar, W. Noell, A. Oudalov, C. Marxer, N. de Rooij, “4x4 & 8x8 Optical Matrix Switch with 250 µm Mirror Pitch”, OMEMS ‘04, Takamatsu, Japan, pp. 162-163.

[12] G. Wallis, D.I. Pomerantz, “Field assisted glass-metal sealing”, J. Appl. Phys. 40, 3946–3949, 1969.

[13] P. Gueulle, “Transformerless DC-DC converter”, electronic Design; October 23, 1997.

4 Technological Realisation

The fabrication process of the MEMS part was introduced in the previous chapter. The required precision of the fabrication of the torsion beams on the backside and the vertical mirrors on the frontside of the silicon wafer caused a large optimisation effort for the etching processes. Due to the double-sided etching approach wafers with a thickness of 120 µm have been used. This caused additional precautions for some existing processes.

In contrast, the fabrication of the microlenses is very simple. It does not need a clean room environment and is compatible to mass production.

4.1 MEMS Actuator

4.1.1 Etching of the Torsion Beams

According to the simulations, the torsion beams need to have a cross section smaller than 1x1 μm^2. Structures of this size are very difficult to fabricate using standard lithography and mask aligners. Additionally, the beams need to be protected from any following fabrication step, especially from the etching of the vertical mirrors. Therefore, torsion beam widths of 5 µm were initially designed on the mask. To reach the exact beam shape that

is required for the application the beams were thinned by consecutive oxidation and HF vapour phase etching.

The combination of DRIE, passivation and isotropic etching is an ideal process to create narrow structures in bulk silicon. The detailed schematic of the beam fabrication process is shown in figure 4.1.

Step a) (thick SiO_2 patterning), b) (DRIE) and c) (thin oxidation) are standard processes in microfabrication. It is important that the thermal SiO_2 that is grown during step c) is much thinner than the SiO_2 on the wafer surface. Under this condition the thinner floor SiO_2 in the etched groove can be etched without affecting the silicon of the wafer surface. This can be done by slightly modifying the DRIE process used to etch the grooves. Then, the structures can be underetched using an isotropic etch step. Again, this was carried out in the DRIE reactor by modifying the process in a way that no passivation layer was deposited.

The following SEM images illustrate the difficulties that were encountered during the development of the process. Figure 4.2 shows a SEM micrograph of the etched platform after step e). To inspect the etching progress in vertical direction the wafers were broken before being investigated in the SEM. The thick and the thin SiO_2 can be seen clearly. The anisotropic etching step was carried out without any problems. An inconvenience appeared after the floor- SiO_2 removal and the following isotropic etching step. After a short etching time, an unwanted undercut at the edges on the wafer surface appeared. A possible reason was suspected to be a charging of the sharp dielectric corners that were formed after the DRIE

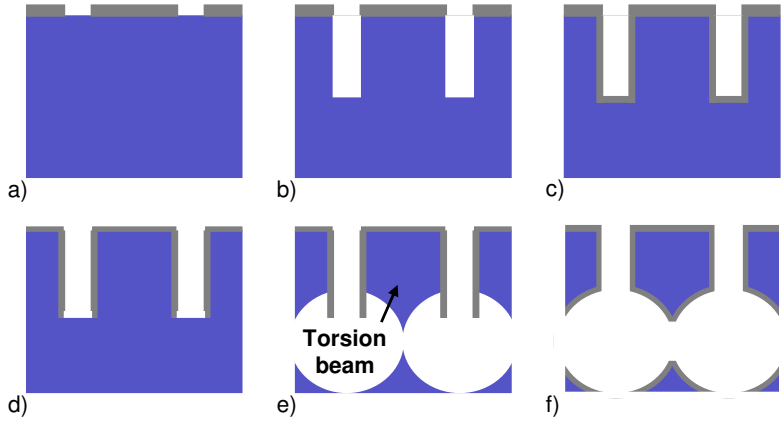

Figure 4.1: *Detailed description of the torsion beam fabrication.*

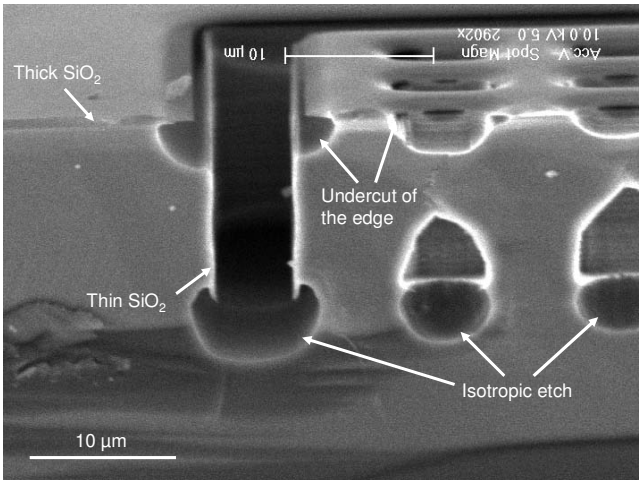

Figure 4.2: *Side-view of the wafer after step e). Besides the thick and thin SiO_2 and the isotropic underetching of the platform, an undercut of the edges on the topside of the wafer appeared. Charging effects on the sharp corners most probably caused the SiO_2 passivation to break.*

(figure 4.2). The strong electric field at the corners would attract the reactive ions and destroy the passivation of the silicon.

The solution to this problem was found in the etching of tapered edges at the beginning of the DRIE step. This was realized by starting the DRIE with an isotropic etching (no polymer deposition) for an etch depth of approximately 1µm (figure 4.3). The isotropic undercut of the SiO_2 mask followed by the thermal oxidation should lead to the desired result. A part

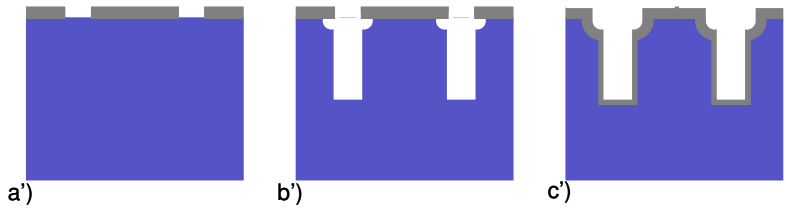

Figure 4.3: *Modified process to avoid the undercutting of the sharp edges on the wafer surface. A short isotropic etching step preceding the DRIE step creates tapered edges that survive the following floor SiO_2 removal step.*

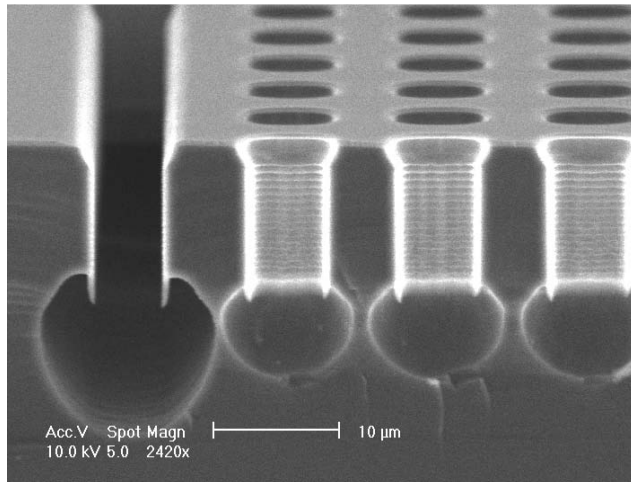

Figure 4.4: *The tapered beginning of the DRIE protects the edges on the wafer surface from being etched.*

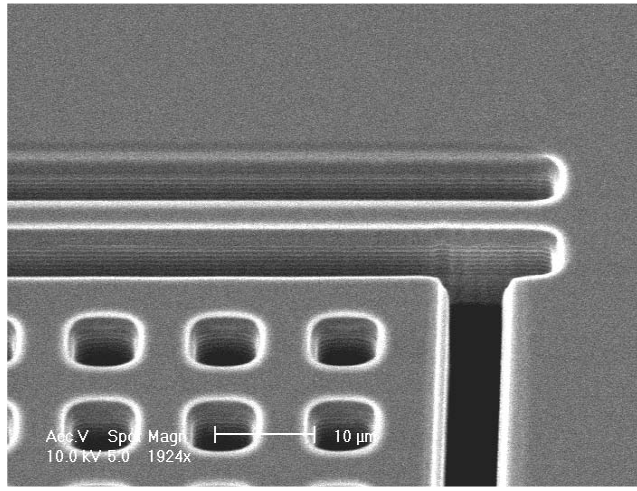

Figure 4.5: *Top view of the torsion beam after step e). The edges of the torsion beam are not undercut.*

of the etched platform is shown in figure 4.4. The protective SiO_2 on the sidewalls is no longer damaged. A large, isotropic undercut of more than 5 µm could be obtained without any degradation of the side-walls.

When looking at figure 4.4, another important process parameter becomes visible: The etching time of the DRIE and the isotropic etching step define the cross section of the undercut structures. A longer DRIE step results in a higher structure, a longer isotropic step decreases the height. Due to the isotropic beginning of the DRIE step the etched beam cross section is more octagonal or round than square. A SEM picture of a part of the torsion beam is shown in figure 4.5.

4.1.2 Etching of the Mirrors

The vertical mirrors were etched on the front-side of the thin wafer. They

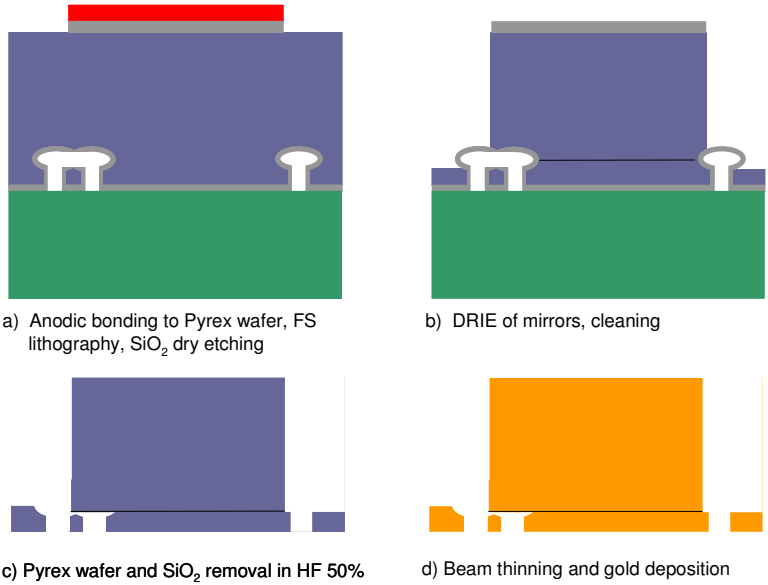

Figure 4.6: *Fabrication process for the mirrors. The fragile silicon wafer is temporarily bonded to a Pyrex wafer, which is then removed with concentrated HF after the DRIE of the mirrors.*

are located in the middle of the platform where the platform is not perforated. This part of the process flow is shown in figure 4.6.

Due to the fragility of the wafer and the deep front-side etching the silicon wafer was anodic-bonded to a 500 µm thick Pyrex wafer with the beams and platforms touching the Pyrex wafer. The bonding parameters have a big influence on the stress between the two wafers and the resulting bow. A high bow (> 100 µm) yields difficulties for processes using vacuum or electrostatic clamping mechanisms and the precision of the photolithography.

The used bonding parameters are shown in table 4.1. Bonding in a vacuum environment would have been preferred because of the following structure opening during the DRIE. However, bows higher than 100 µm have been obtained. Since the enclosed pressure did not harm the structures, the reason behind the strong bowing was not further investigated and the bonding was accomplished under atmospheric pressure.

Table 4.1: *Anodic bonding parameters: The resulting bow is highly influenced by the pressure in the cavities. Best bonding results were achieved at atmospheric pressure.*

Voltage [V]	Contact force [N]	Temperature top/bottom [°C]	Vacuum	Resulting bow [µm]
700	300	365/365	Yes	140
700	300	365/365	No	-30

Due to the protective SiO_2 on the silicon wafer a relatively high bonding voltage of 700 V has been taken.

After bonding, the back-side of the Pyrex wafer was covered with a thin layer of aluminium to allow the electrostatic clamping in the DRIE reactor. A "window" allowing the following backside alignment was created with an adhesive tape glued on the Pyrex wafer prior to the aluminium deposition.

Prior to the lithography the thin SiO_2 on the top-side of the silicon wafer was etched away using RIE. The mirrors were fabricated by DRIE. Often very thin, vertical structures are fabricated using protective dummy-walls surrounding the actual structure. These walls protect the mirror from being underetched. They have to be designed in a way that they can be removed after the etching. This is usually accomplished by designing these walls thinner than the actual mirror and removing them by oxidation and HF etching. This technique caused a lot of problems in this design since these

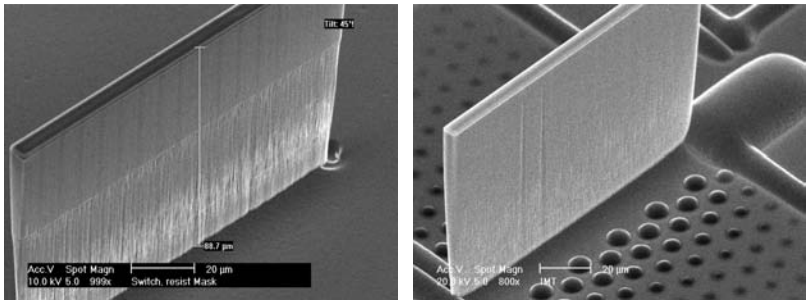

Figure 4.7: *Left: Silicon mirror fabricated without protective walls. The side-wall roughness increased drastically each time the DRIE was interrupted to inspect the wafer. Right: Silicon mirror etched with a long first DRIE step. The mirror quality is good over a much longer depth.*

structures could not be attached very well to the chip and had to be attached to the mirror itself. Instead, a DRIE process enabling us to etch 100 µm high vertical mirrors without protective walls was developed. Figure 4.7 shows a silicon mirror fabricated without protective walls. The left picture shows a mirror that was etched in three steps to monitor the etching process. The side-wall roughness increased drastically each time the DRIE was interrupted to inspect the wafer. A silicon mirror etched with a long first DRIE step is

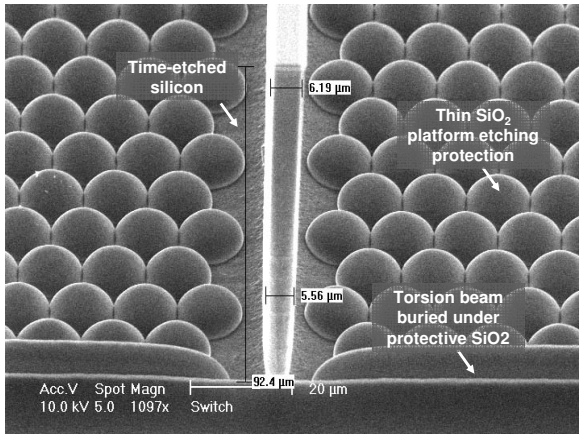

Figure 4.8: *SiO_2 protecting the torsion beams and the platform from the front-side etching. The verticality of the vertical mirror is better than 0.5 degrees.*

shown in the right image. The mirror roughness is constant over a much longer depth.

The torsion beams and a big part of the platform are protected from the deep front-side etching by the thin SiO_2. Nevertheless, the etch depth had to be controlled in order to keep the supporting structures of the chip. Timed etching allowed us to leave a supporting silicon thickness of less than 10 µm. An indicator for the timed etching was the appearance of the thin SiO_2 protecting the torsion beams and the platform. As it can be seen in figure 4.8, the isotropic undercut of the individual holes in the platforms are touching, forming a continuous layer of SiO_2. The verticality of the mirror is better than 0.5 degrees. The mirror itself is anchored by a region without SiO_2 in the middle of the platform.

The fabrication yield is most influenced by the timed etching. If the etching is too short the platforms are not released or the remaining silicon on the SiO_2 will get in the way of the movable structures. If it is too long the supporting frame for the torsion beams and optical fibers will be too weak or even etched away. A "natural" overetching failure rate is caused by the total thickness variation of the wafer and the etch non-uniformity of the DRIE process.

At that stage the general shape of the actuator is fabricated. The Pyrex wafer is removed by concentrated HF. The approximately 4 µm thick torsion beams allow for a last piranha cleaning and water rinsing before all the structures are thinned by consecutive thermal oxidation and HF vapour etching. The targeted torsion beam thickness of 1 µm can be achieved if the SiO_2 is etched in a HF vapour atmosphere. A part of an 8x8 mirror matrix is shown in figure 4.9. The platforms are only suspended by torsion beams, which have a cross section of less than a micrometer. The shape of the torsion beam appears to be round but can't be determined exactly. The shape is due to the isotropic beginning of the beam-etching and the thermal oxidation, which is known to round the sharp edges. Torsion beams with a diameter of down to 0.5 µm and length of 150 µm were fabricated.

The secondary effect of the rounding effect is a decrease of the mirrors surface roughness. An image of a complete 8x8 cross connect is shown in figure 4.10. The chips can be released from the wafer by breaking the four beams holding the individual chips on a stable grid.

A thin layer of gold is sputtered on the individual chips to assure a high reflectivity in the infrared band. A gold layer of 60 nm results in a reflectivity of better than 97.5 % for normal incidences[1]. The sputtering equipment did not allow for a precise measurement of the deposited layer.

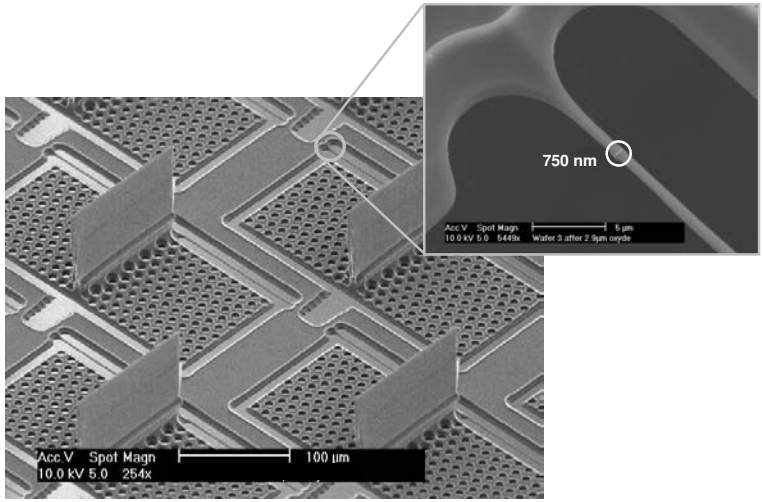

Figure 4.9: *A part of an 8x8 mirror matrix. The freestanding platforms are only suspended by the thinned torsion beams.*

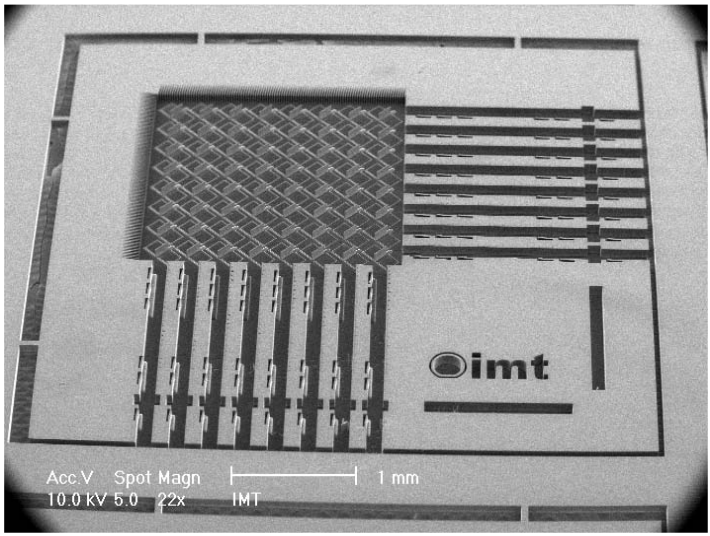

Figure 4.10: *Complete 8x8 cross connect with mirror matrix, fiber alignment structures and break beams for dicing free release of the chips.*

4.2 Microlenses

In comparison to the mirror matrix the fabrication of the GRIN lenses requires only a minimal set of equipment when compared to the conventional methods used for the fabrication of GRIN lenses. The fabrication sequence is plotted in figure 4.11. The first step is the dicing of V-grooves in the silicon substrate. This is done by means of a V-shaped dicing blade and a wafer dicing machine. Then, the fibers are cut to appropriate lengths and inserted into the V-grooves. The fibers are fixed by means of thermal glue.

The glue has to match a number of requirements, the foremost being the ease with which it can be removed. For the current application, a thermal glue (STEPWAX No. 1) was used. This glue has the property of turning to a liquid when heated to a certain temperature and solidifying again when cooled. Best results were obtained by heating the silicon wafer on a hot plate to 130°C. The glue is then spread over a second wafer which is then pressed on top of the first one carrying the GRIN fiber pieces in the grooves. This ensures a good penetration of the glue into the grooves as well as an extra mechanical fixation for the fibers.

After the glue has cooled down the lenses can be fabricated. The fabrication utilizes the same dicing machine that was used for the creation of the V-grooves. GRIN rod pieces of defined length are cut by dicing in the perpendicular direction to the fiber pieces (figure 4.12). The x-step distance of the dicing machine is composed by the desired lengths of the GRIN lenses plus the width of the dicing blade.

In order to have a small surface roughness on the diced lenses a fine diamond blade with grit size of 3 to 6 µm was taken.
Based on the microscope image of the lens one can conclude that a rather high degree of surface roughness is present. This is confirmed by an SEM image of the lens (figure 4.13 a)) and an AFM measurement indicating an RMS roughness of over 1 µm. Such a degree of surface roughness does not necessarily mean that the lens will not operate in index matched fluid. Since the optical rays do not experience a refractive index variation at the lens-fluid interface losses due to scattering can be avoided. However, operation in air will be accompanied with high losses.

In order to reduce the surface roughness a number of approaches have been investigated. One is based on etching the GRIN lenses in a hydrofluoric acid solution. The reasoning behind this is that although the acid will etch the fiber isotropically, the rougher outer edges will most likely be smoothed out by the process. The fibers were fixed by photoresist and not by glue that dissolve faster in the acid. After being etched for 10 minutes in BHF an AFM

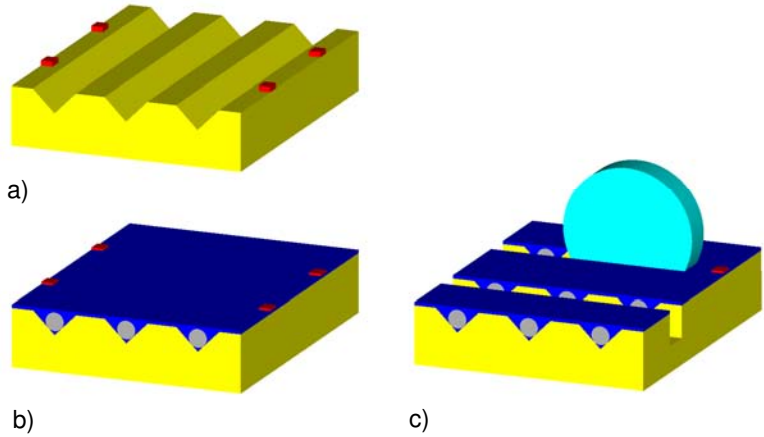

Figure 4.11: *Fabrication sequence for GRIN lens rods: a) dicing of the V-grooves, b) gluing of the GRIN fiber pieces, c) dicing of the GRIN lenses.*

measurement of the fiber indicated a slightly lower surface roughness. Based on these AFM measurements, one would suspect that there is an improvement of the flatness. However, inspection under an optical microscope leads to a different conclusion.

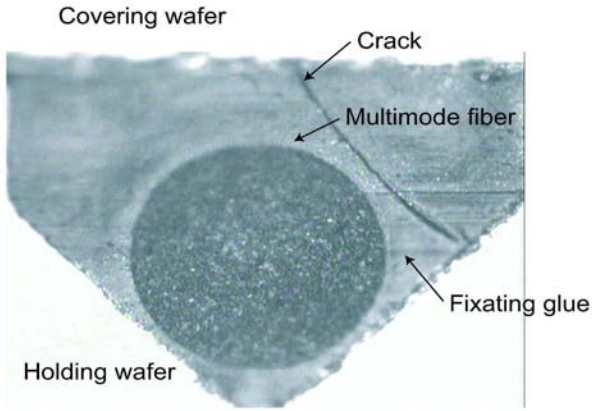

Figure 4.12: *Surface roughness of the GRIN lens after dicing. The roughness was measured to be about 1 µm RMS.*

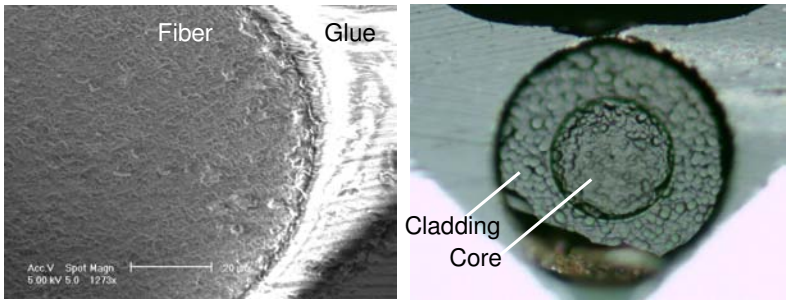

Figure 4.13: *a) AFM image of a diced GRIN lens after dicing. b) GRIN lens after etching for 60 minutes in BHF. The crater-like surface is probably caused by micro-cracks in the glass after dicing.*

On the micro-scale the edges have indeed been smoothed out, whereas on the macro scale a very clear deterioration of the surface is visible. A moon crater landscape with significant height variations was created, probably due to micro-cracks in the glass (figure 4.13 b)).

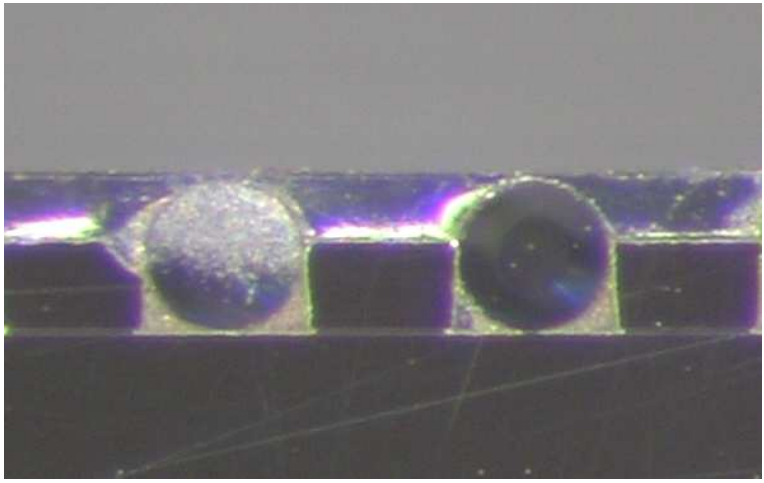

Figure 4.14: *GRIN lens before (left) and after (right) mechanical polishing.*

A different solution to the roughness problem is mechanical polishing of the endfaces. This technique has yielded very good results with regard to the surface roughness (figure 4.14). However, the fixation of the lenses during the polishing or the precise control of the length of the lens is very difficult. Moreover, this process, although suitable for small batches, does not meet the requirements of mass production.

4.3 OXC

To complete the fabrication of the OXC an electrode chip and a spacer had to be microfabricated. The fabrication of the electrode is straightforward: A thin (500 nm) layer of aluminium is evaporated on a Pyrex wafer. Then the desired structured can be patterned in a wet etchant using a photoresist mask. The result is shown in figure 4.15.

Spacers were also fabricated out of 200 µm thick Pyrex wafers covered with a 400 nm thick LPCVD poly-silicon layer. The poly-silicon is patterned by RIE using a photoresist mask. The Pyrex is etched using a concentrated HF solution. Because of the thinness of the Pyrex, wafer dicing becomes difficult. Therefore, the individual spacers were directly etched into separate parts in the HF acid.

4.3.1 Assembly

The high number of single parts of the OXC makes the assembly difficult and time consuming. However, the compactness of the chip justifies the effort. Passive alignment features and parallel assembly were a key subject already during the designing phase.

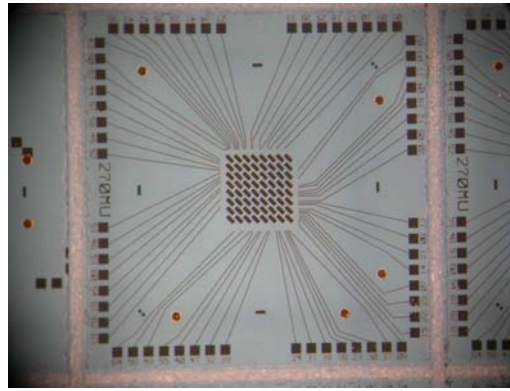

Figure 4.15: *Diced 8x8 electrode chip. The aluminium electrodes are etched on a Pyrex substrate.*

The most important step is the assembly of the fragile silicon actuator chip to the spacer. Pyrex is the preferred material for the spacers since it enables the use of anodic bonding to bond the two parts. The big advantage of anodic bonding is that it is possible to create a stress-free bond and it does not need any intermediate adhesive layer between the two parts. The result is a durable, flat connection between the spacer and the actuator chip.

The chipwise anodic bonding was performed on an electrically conductive hotplate (on ground potential) with the silicon chip on the bottom. The spacer was aligned under an optical microscope using a homebuilt XYZθ-stage and a vacuum tool which was directly used as positive electrode. The bonding temperature was 365°C, the required bonding voltage was around 800 V and the bonding time was one minute.

The strengthened actuator was then aligned and glued to the electrode chip that was previously connected to a printed circuit board by wirebonding (figure 4.16). The higher rigidity allowed the use of UV-glue.

A semi-automated positioning stage was used to place the tiny GRIN lens rods onto the chip. A special vacuum tool able to pick up individual GRIN lenses had to be fabricated and facilitated the handling (figure 4.17). The GRIN lenses were positioned under a microscope and pushed into the U-groove on the silicon chip. The mechanical springs, etched on the chip, clamp the lenses (see figure 4.18). This prevents the lenses from sticking to the vacuum tool due to electrostatic forces. The vacuum tool can then be removed and is ready to pick up the next lens.

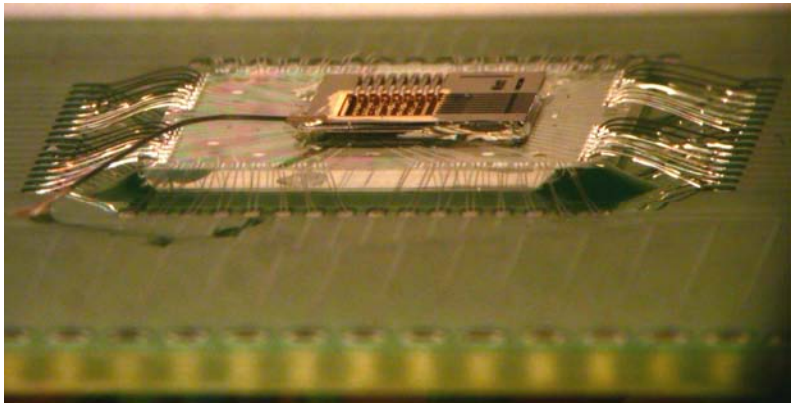

Figure 4.16: *Anodic bonded spacer-actuator chip and electrode chip, glued and wire-bonded to a printed circuit board.*

The cleaving of the fiber ribbons was made with a commercial tool. The insertion and positioning was accomplished with a Z-stage whereon the ribbon could be fixed temporarily. The individual GRIN lenses were pushed in place by the ribbon until they touched the stoppers at the end of the fiber channels. Then, the ribbon was retracted by the desired distance between SMF and GRIN lens. A microfabricated ruler between the U-grooves could be used to control the positioning (figure 4.18).

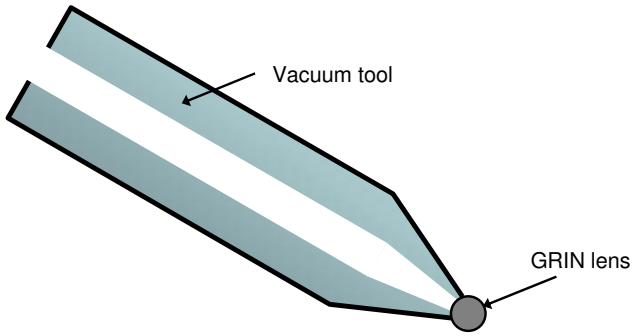

Figure 4.17: *A special vacuum tool able to pick and place the lenses using a semi-automated micropositionner.*

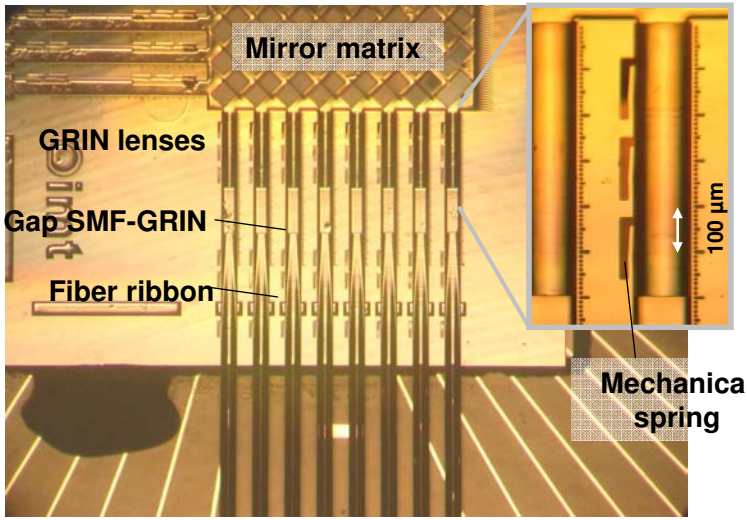

Figure 4.18: *U-grooves with assembled GRIN lenses, fiber ribbon, mechanical holding springs and ruler to control the positioning.*

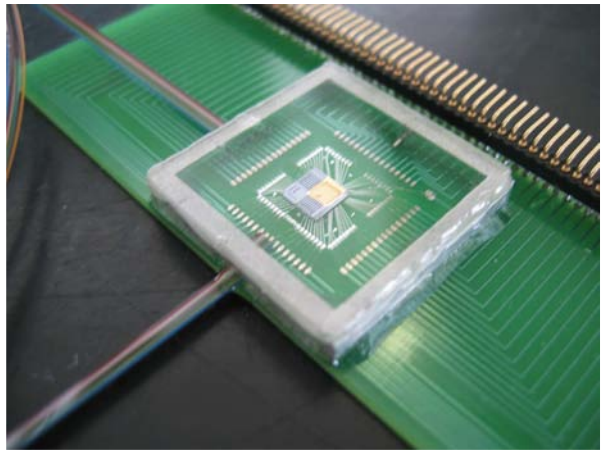

Figure 4.19: *Assembled 8x8 OXC on the PCB. An aluminium frame is glued on the PCB, filled with index matching oil and sealed by a glass plate and epoxy glue.*

An aluminium frame amply surrounding the chip is glued on the PCB. After filling the chip area with index matching fluid a glass lid is glued on top of the frame and sealed with epoxy glue. A picture of an assembled 8x8 cross connect is shown in figure 4.19. To complete the assembly the electrical contacts of the PCB have to be wired to the high voltage electronics.

References:

[1] C. Marxer, “Silicon Micromechanics for Application in Fiber Optic Communication”, Dissertation, University of Neuchatel, 1997, pp. 88-89.

5 Characterisation and Discussion

This chapter outlines the measurements of the microfabricated parts. First, the performance of the MEMS actuator and the GRIN lenses are measured separately and compared to the simulated results. Then, the coupling performance of an assembled 4x4 and 8x8 OXC is shown.

5.1 MEMS Actuator

The fragility of the silicon actuators requires a careful treatment during the fabrication and characterisation process. The large deflection angle of the actuators and the porous surface of the platform make the choice of the right observation mechanism difficult. On the other side, the binary-operation of the optical switch limits the number of interesting characteristics to the values measured hereafter.

All measurements characterizing the mechanical properties of the switch were carried out without index matching fluid, which would constrain the choice of measurement equipment.

5.1.1 Actuation Voltage

The actuation voltage depends very strongly on the beam cross section. To characterize the exact actuation voltage dependency on the beam shape the dimensions of the beam itself would have to be characterized with high precision, which turned out to be very difficult. The small dimensions in the order of one micrometer and the rounded edges of the beams make it impossible to determine the exact beam cross section without destroying the chip. The most accurate way is inspecting the torsion beams in the SEM (figure 5.1). Therefore, I want to focus more on the voltage-theta characteristic and only give an estimate for the voltage - beam thickness dependency.

Another inconvenience of the thin beam section is the strong dependency to process variations and mask tolerances. A small variation of the beam thickness causes a relatively large actuation voltage change. A variation of a factor of two between lowest and highest actuation voltage was observed on most of the 8x8 OXC.

A measured voltage-theta characteristic of an actuator with estimated torsion beam diameter of 0.8 µm is shown in figure 5.2 and compared to the simulation result for torsion beams with a square section of 0.8x0.8 μm^2 using the energy method. The shape of the curve agrees very well with the simulation, which is another indication for the good performance of the simulation method. The spring constant of the real torsion beam is presumed to be smaller due to the rounding of the sharp edges. The latter explains a lower actuation voltage than simulated.

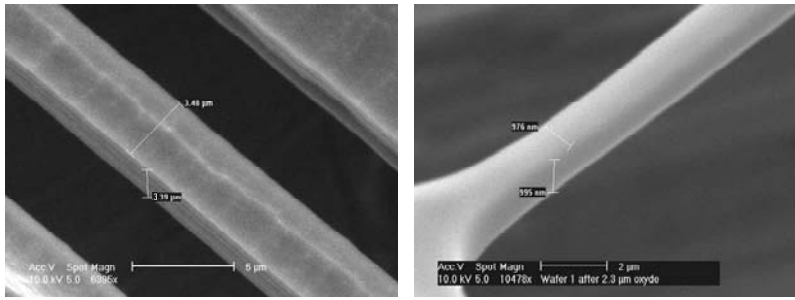

Figure 5.1: *Left: Torsion beam before thinning. Right: Torsion beam after thinning. The exact cross section can not be determined by SEM inspection but a rounding of the sharp corners can be observed.*

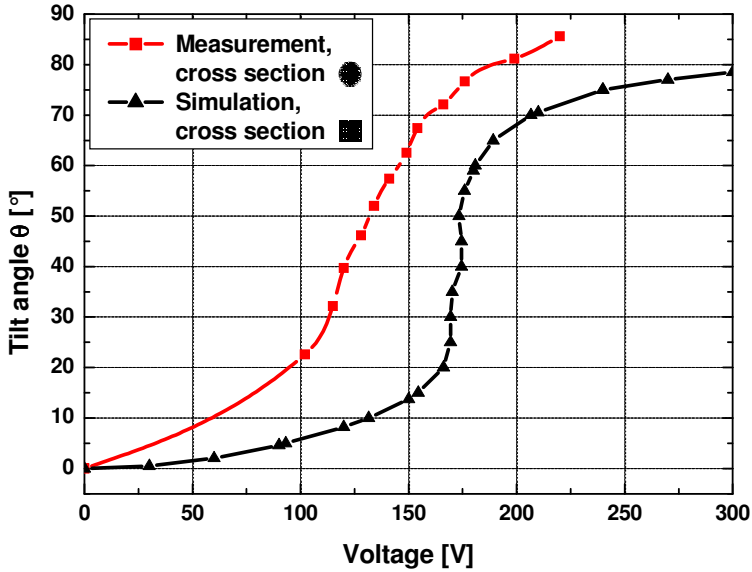

Figure 5.2: *Comparison between the measurement of an actuator with estimated torsion beam diameter of 0.8 µm and the simulation with torsion beams having a cross section of 0.8x0.8 µm² using the energy method. The spring constant of the real torsion beam is presumed to be smaller due to the rounding of the sharp edges. The latter explains the smaller actuation voltage.*

5.1.2 Switching Speed and Resonance Frequency

The resonance frequency of different actuators on one 8x8 chip was measured with a Doppler laser vibrometer. The measurements for four actuators are given in figure 5.3. Additionally, the corresponding voltages, at which the actuators started to tilt, were measured by visual inspection under a microscope. The cross sections of the beams were measured to be in the order of 1x1 µm².

A clear relation between resonance frequency and actuation voltage can be seen in figure 5.3. The relation between resonance frequency and the voltage that is needed to actuate the platform to a certain angle θ can be calculated. The resonance frequency of a torsion pendulum is given by

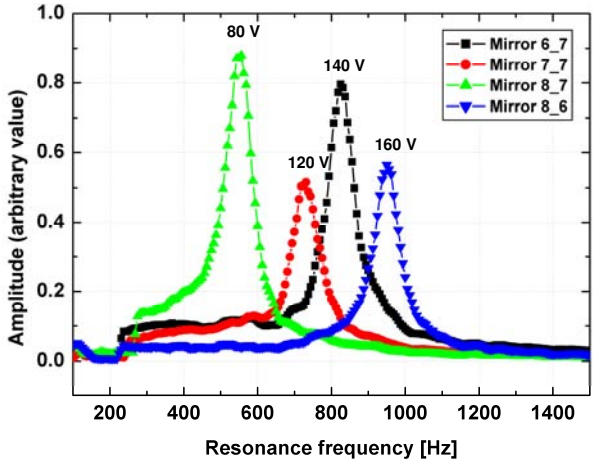

Figure 5.3: *Resonance frequency for different actuators on one 8x8 chip. The high variation of the resonance frequencies reflects the variation of the actuation voltage.*

$$f_{res} = \frac{1}{2\pi}\sqrt{\frac{D}{J}} \tag{5.1}$$

where D is the torsion coefficient and J is the moment of inertia. The platform of our actuator can be described as a pendulum, which is suspended by the torsion beams. The moment M, which is applied to the torsion beams is given by

$$M = D \cdot \theta \tag{5.2}$$

where θ is the torsion angle . From equation 5.2 we obtain

$$D = \frac{M}{\theta}, \tag{5.3}$$

which can be inserted into equation 5.1

$$f_{res} = \frac{1}{2\pi}\sqrt{\frac{M}{\theta \cdot J}}\ . \tag{5.4}$$

The electrostatic torque on the platform can be expressed by

$$M = \frac{1}{2} V^2 \frac{\partial C}{\partial \theta} \tag{5.5}$$

where C is the capacity of the actuator, which only depends on the geometry of the actuator and not of the applied voltage. If equation 5.5 is inserted into equation 5.4 we obtain

$$f_{res} = \frac{1}{2\pi} \sqrt{\frac{\partial C / \partial \theta}{2 \theta J}} V_{\theta}. \tag{5.6}$$

The variation of the capacity at a given angle θ is constant. If we measure the resonance frequencies of different actuators and compare these values to the actuation voltages at a constant angle we should see a linear dependency of f_{res} and the corresponding actuation voltage V_{θ} of the actuator. Note, that equation 5.6 does not mean that the resonance frequency is changing with the applied voltage.

These values were measured for a number of actuators from the same wafer and are plotted in figure 5.4. The actuation voltage was determined by observing the actuator under a microscope, which explains the variation of the measurements to the linear fit. However, a clear linear dependency can be seen in the graph. Since the resonance frequency can be determined at very small excitation voltages, its measurement can be used as a minimally invasive determination of the actuation voltage.

The measurements shown in figure 5.4 reflect a high variation of the actuation voltage distributed over a single 8x8 chip. This implies that either each actuation voltage for the 64 actuator has to be calibrated individually or that all actuators have to withstand the highest needed actuation voltage. Since the measurements showed that a higher actuation voltage does not harm the thinnest beams on a chip, the second and simpler method was implemented.

Figure 5.5 shows a resonance measurement of the supporting grid holding the actuators. The measurement was carried out by actuating all the mirrors in parallel to have the highest possible force on the grid. Resonance frequency peaks are visible below 500 Hz and at 3.4 kHz. The oscillation amplitude is about 200 times smaller than the oscillation of the actuators and should not influence the optical performance of the device.

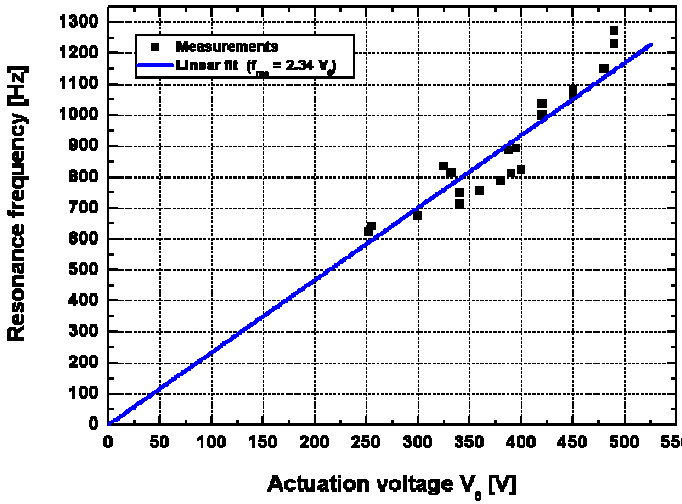

Figure 5.4: *Resonance frequency of the platform vs. actuation voltage. The actuation angle was determined under a microscope. A clear linear dependency can be seen in the graph.*

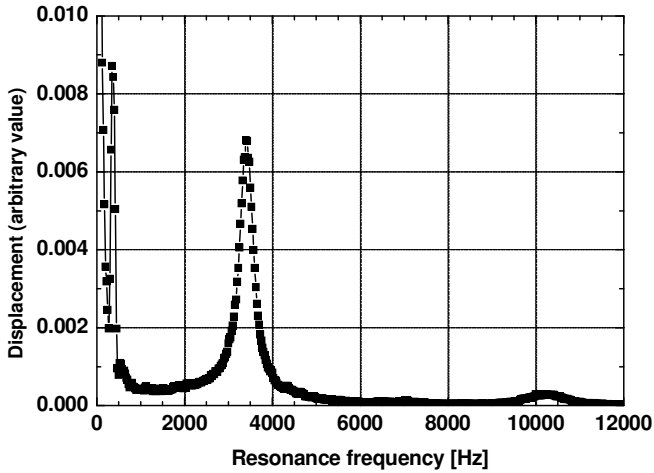

Figure 5.5: *Resonance frequencies of the supporting grid holding the actuators. Peaks are visible below 500 Hz and at 3.4 kHz. The oscillation amplitude is about 200 smaller than the oscillation of the actuators.*

The switching speed of an actuator in oil was measured optically by using the reflected signal of a mirror. A measurement is shown in figure 5.6. It is worth noting that the mirror moves down when the actuation voltage changes to the high state. The photodiode generates a negative voltage upon receiving light, thus, a low state corresponds to a mirror being flipped up.

The actuation frequency was 100 Hz. The switching speed to release the mirror (t_{on}) was less than 1.5 ms. Some ringing was observed but could be minimized with an optimized actuation voltage. The time to pull the mirror down (t_{off}) was less than 3 ms. A clear delay in the reaction of the mirror can be observed, which is probably caused by the high RC value of the electrical driving circuit and will have to be examined in the future. At an actuation frequency of 200 Hz the two states of the mirror can still be separated clearly.

Figure 5.6: *The switching speed of the OXC in oil was determined by the measurement of the reflected optical signal. Left: Actuation at 100 Hz. t_{off} is larger than t_{on}, which is probably due to the large RC value of the electrical circuit causing a slow charging of the electrode. Right: Actuation at 200 Hz.*

5.2 GRIN Lenses

The surface roughness of the non polished GRIN lenses is too high to be considered as a good optical element. An optically flat surface should have a roughness smaller than the wavelength of the processed light divided by 20. It is evident that the coupling losses of an optical element with such a surface will be high due to the scattering of the light. The question now is what is the influence of the surface roughness if the GRIN lenses are surrounded by a material having a similar refractive index? Are the losses only noticeable in the presence of surface roughness and refractive index mismatch?

5.2.1 Measurement Setup

The basis of the measurement setup was formed by a set of straight rectangular U-grooves etched into a silicon wafer. The grooves had the width of an optical fiber. A set of microfabricated springs on the walls of the grooves ensured precise alignment. The GRIN lenses were positioned into the grooves by means of the micro-assembly stage and the special vacuum tool. The stage was equipped with a microscope. The lenses were placed manually into the grooves. Finally, when both the fibers and the GRIN lenses were in place, a glass lid was placed on top and gently loaded with a needle. This ensured that the components were all tightly in place. An overview of the setup is given in figure 5.7.

Initially, the GRIN lenses were placed as far apart as possible. The length of the free space region between the lenses could then be tuned by pushing the lenses with the SM fibers. However, the lenses can only be pushed in one direction. By retracting the fibers we could precisely determine the length of the SMF-GRIN lens gap. The precision of this movement was estimated to be in the order of 10 μm. The actual distance between the GRIN lenses was determined by means of a ruler present in the microscope above the setup with a precision of 50 μm.

The experiment was performed in index matching fluid covering the whole assembly. The fluid decreases Fresnel reflection losses that are due to a mismatch of refractive index between two surfaces. Additionally, the surface roughness of both fibers and GRIN lenses were smoothed out by the oil.

The output signal was measured by a photo detector that was previously calibrated in order to provide the value of the insertion loss.

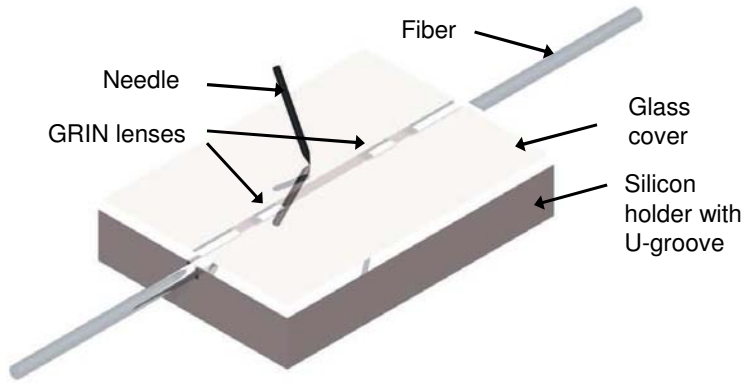

Figure 5.7: *Measurement setup for the GRIN lens characterisation: Two GRIN lenses are placed into a U-groove. A glass cover plate ensures the vertical alignment. The lenses are pushed to the desired location with the optical fibers that are fixed to a translation stage.*

5.2.2 Results

The simulations indicate that the length of an ideal GRIN lens is dependent on the gap size used between the lens and the SMF. The paraxial simulation for a fixed gap size of 250 µm between the GRIN lens and the SMF is shown in figure 5.8 a). A typical example of a measured GRIN lens collimator is shown in figure 5.8 b). The measured values agree well with the simulations. The length of a GRIN lens that yields the lowest cumulative losses of the required working distance is 645 µm according to the measurements and 650 µm according to the simulations. A typical "window" where the collimator scheme operates well is clearly visible. The measurements carried out for different gap sizes and GRIN lens lengths exhibit similar behaviour and good agreement with the simulations.

For the gap size of 350 µm the optimal GRIN lens length has been found to be 610 µm. The measured losses for different coupling lengths are shown in figure 5.9. In the same plot, the performance of a 645 µm long GRIN lens with a gap size of 250 µm is shown. In agreement with the simulations, the

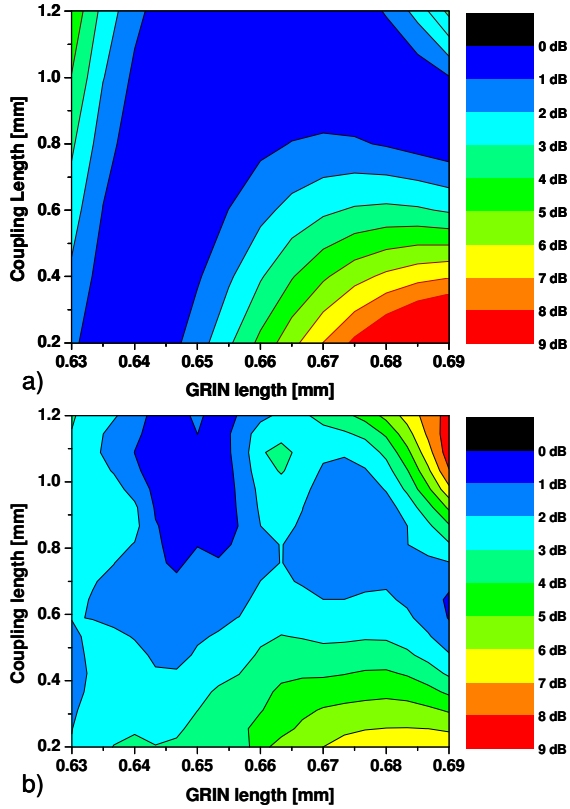

Figure 5.8: *Comparison between simulations and measurements of the GRIN lenses in index matching oil: a) Simulation of the losses with a gap size of 250 µm , b) measured losses of the collimation setup with gap size of 250 µm.*

longer GRIN lens features lower insertion losses for a narrow operating region. However, the overall cumulative losses of the shorter lens are lower. It seems that although the optical beam in the GRIN lens extended the size of the core, no substantial loss is observed. To further confirm this claim even shorter GRIN lenses have been taken whereas the gap size has been increased to above 350 µm. A GRIN lens with a length of 595 µm and a gap size of 400 µm has been fully characterised. The losses of the setup remained remarkably constant in the range of 1.3 – 2.0 dB for coupling lengths of 0.2

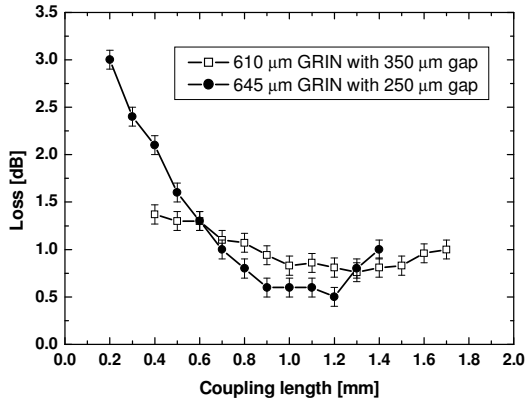

Figure 5.9: *Comparison of the losses for two different GRIN lens and gap lengths. Even though the beam diameter exceeds the GRIN lens core the setup yields low losses over a large coupling length.*

to 2 mm. It is likely that light is reflected at the core-cladding interface causing smaller losses as predicted. Therefore, taking a fiber with a substantially bigger core, i.e. smaller cladding, would enable efficient coupling over even longer distances.

Finally, I would like to note the relationship between surface roughness and the observed losses deduced from the experiments. As stated above, the collimator setup was immersed into index matching fluid that virtually eliminated all negative consequences of surface roughness. The latter can be concluded from the fact that the best insertion losses measured with the lens collimating setup were only 0.3 dB. Butt-to-butt coupling of two single mode fibers in the same grooves yielded insertion losses of 0.15 dB. The excess loss contributed by the lenses is therefore only 0.15 dB. Spreading this loss over the 4 interfaces of the lens means that each one contributes a negligible amount of loss. However, once a similar experiment was carried out without the presence of oil, the losses rose dramatically. With oil a measured loss was 3.6 dB for a certain setup. Without oil the loss increased to 8 dB.

5.3 OXC

The large number and the small size of the different components needed to fabricate the complete optical cross connect requires a number of special tools to handle and assemble the parts. These tools as well as some training of the operating person keep the failure rate relatively low. The good functionality of the optical cross connect is governed by the cooperation of optical, mechanical and electrical parts each having proper failure modes. The assembly and alignment of the component add another type of failure mode, which makes it very difficult to find the origin of sub-optimal measurements.

5.3.1 Measurement Setup

To measure the 8x8 matrix switch 64 high voltage channels need to be controlled in parallel. The control was implemented on a personal computer, which generated a 6 bit signal encoding the desired switching pattern. This signal was decoded electronically by a multiplexer, controlling 64 high voltage transistors on a PCB. To increase the throughput of tested chips a ribbon connector was used to connect the PCB hosting the MEMS chip.

Eight laser sources operating around a wavelength of 1.55 µm were connected to the input fiber ribbon. The output fiber ribbon was connected to eight calibrated monitor diodes measuring the coupling loss of each channel. A schematic of the complete setup is shown in figure 5.11.

The GRIN lenses have a considerable contribution to the coupling loss, which is dependent on the optical path length the light has to travel. The calculated losses for the fabricated GRIN lenses with a core diameter of 62.5 µm are plotted in figure 5.12. For different gap lengths between SMF and GRIN lens the optimal GRIN lens length was taken to make the plot. For the largest coupling length a gap of 300 µm and a GRIN lens with a length of 610 µm yielded a loss of about 9 dB that originated only from the mismatch of the diameter and the curvature of the optical beam. Losses due to diffraction, surface properties, beam clipping and misalignment will add to this value.

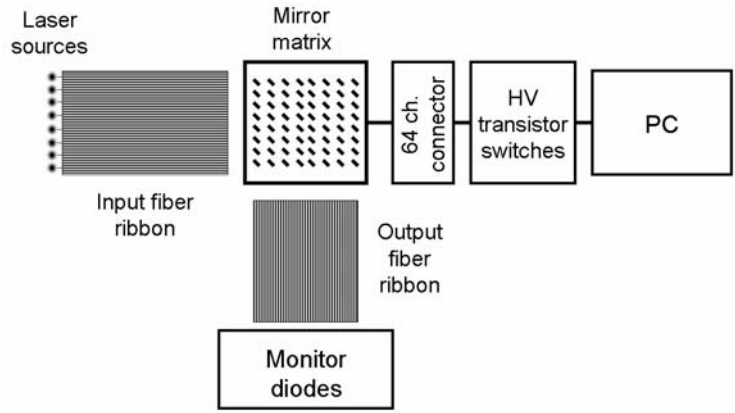

Figure 5.11: *Setup for the characterisation of the optical cross connects. The controlling of the 64 mirrors is implemented on a PC. Eight laser sources and diodes enable a fast measurement of the mirror matrix.*

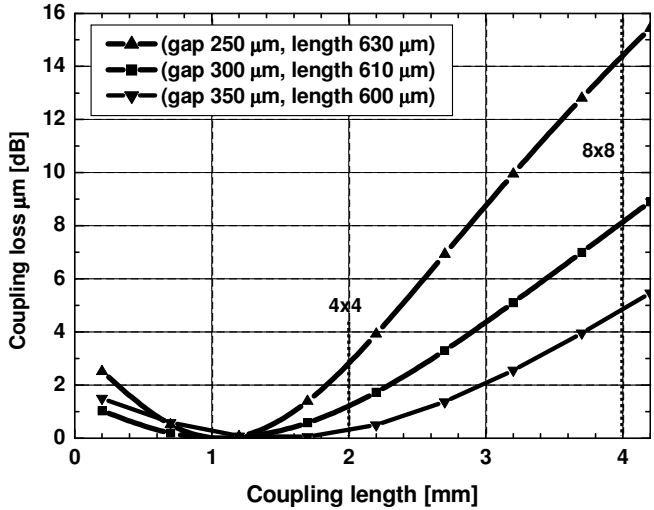

Figure 5.12: *Calculated intrinsic losses of the GRIN lenses for the different coupling lengths. Diffraction, scattering, beam clipping and misalignment losses will add to these values.*

5.3.2 Optical Characterisation of the 4x4 Optical Cross Connect

The handling of the 4x4 switches is less critical than the 8x8's. A measurement of a complete matrix is given in table 5.1. The bold numbers on the left indicate the number of the input channels while the numbers on the bottom indicate the output channel. The dash means that the value could not be measured. The reason was a broken mirror, fiber or GRIN lens.

Table 5.1: *Measured optical losses of a 4x4 mirror matrix in dB.*

4	-	5.7	3.1	2.8
3	-	5.1	9.0	16
2	-	11	12	13
1	-	15	-	12
dB	**1**	**2**	**3**	**4**

The measured coupling losses were significantly higher than expected. However, the channel with the longest optical path yielded a loss of only 2.8 dB, which is close to the optical loss of the collimating system itself. Some electromechanical cross talk was observed. The switching of a mirror influenced the neighbouring mirrors. This is not problematic if the neighbouring mirror moves only for a small vertical distance. However, if the mirror is rotated around its vertical axis by the actuation of neighbouring electrodes this will result in an additional coupling loss.

To avoid any influences of the actuation a 4x4 chip was prepared in order to have only a diagonal matrix of mirrors left. With this setup four non-actuated channels could be measured with no voltage applied. The result is shown in table 5.2. A relatively constant loss of 2 to 3.6 dB was measured for similar coupling lengths. This means that a variation of the coupling losses in the order of 2 dB comes from the assembly and the quality of the optical surfaces.

Individual channels on other chips yielded a loss of only 1 dB, which is close to the theoretical limit of the optical system. The latter proves that the quality of the mirrors is excellent and the optimization of the chip performance should be focused on the actuation of the mirrors and the alignment of the micro-optical components.

Table 5.2: *Measured optical losses of a 4x4 mirror matrix prepared in order to have only diagonal mirrors left. With this setup a set of non-actuated mirrors could be measured to study the influence of the electromechanical cross talk.*

4	2.7	-	-	-
3	-	2	-	-
2	-	-	3.6	-
1	-	-	-	3.5
dB	**1**	**2**	**3**	**4**

5.3.3 Optical Characterisation of the 8x8 Optical Cross Connect

The larger area of the switch matrix and the supporting grid drastically decrease the mechanical stability of the chip and favour the electromechanical cross talk. The larger coupling lengths make it susceptible to angular misalignments of the GRIN lenses. The measurements of an 8x8 mirror matrix are shown in table 5.3.

Table 5.3: *Measured optical losses of an 8x8 mirror matrix. Some channels yielded very high, other channels low losses. The distribution of losses less than 8 dB (highlighted) and the values over 20 dB indicate that the losses originated from a bad alignment of the assembled optical components.*

8	15.50	18.11	5.43	21.27	15.29	7.34	30.0	6.84
7	26.70	22.47	15.80	30.01	28.00	32.00	55.5	23.18
6	13.15	14.35	9.35	15.99	14.86	14.53	40.0	15.77
5	5.98	8.87	5.28	10.54	9.11	5.53	40.0	8.12
4	5.24	9.50	4.41	12.24	11.08	3.78	30.81	5.49
3	7.18	8.05	4.71	10.51	9.52	3.22	26.29	21.00
2	3.90	6.20	3.60	9.87	10.22	2.89	26.22	3.60
1	4.70	6.50	3.60	8.90	10.80	3.76	35.70	2.78
dB	**1**	**2**	**3**	**4**	**5**	**6**	**7**	**8**

At first glance a variety of different values ranging from 2 to 55 dB are visible. The interesting thing that can be seen in this measurement is that

some channels yielded very high losses while other channels yielded low losses. For example, input 7 and output 7 showed losses around 30 dB. Mirror 7_7 yielded 55 dB, which indicates that the loss originated from the alignment of the fibers or the GRIN lenses at input 7 and output 7. The elements of input 1, 2, 4, 5, 8 and output 1, 3, 6, 8 seem to be very well aligned since the mirrors switching these channels showed losses smaller than 6 dB. An outstanding performance showed mirror 8_8 with a coupling length of 4 mm. 6.84 dB is very close to the theoretical limit of the GRIN lenses.

Another measurement was done with a chip where the optical components were actively aligned. After the assembly of the chip the fiber ribbon cable was aligned in a way to get a constant optical performance over the whole matrix. The result is shown in table 5.4. After assembly, all the mirrors were functional. During the electromechanical testing some mirrors broke before being measured optically. Broken mirrors are indicated by a dash.

Table 5.4: *Measured optical losses with active alignment of the fiber ribbon. The losses are constant and lie roughly between 6 and 12 dB.*

8	-	6.5	5.7	6.3	7.5	7.9	8.9	10.9
7	4.5	6.5	7.9	8.8	9.6	10.4	9.8	13.5
6	7.2	9.1	10.4	9.9	11.2	10.7	13.3	13.3
5	6.5	8.0	8.6	9.3	10.1	10.0	12.4	12.0
4	7.5	9.8	8.9	9.5	11.1	10.2	11.7	12.4
3	9.7	10.7	10.3	10.2	11.2	11.1	-	-
2	12.7	13.9	14.1	12.8	12.6	13.4	-	-
1	10.1	11.1	12.0	-	-	-	-	-
dB	**1**	**2**	**3**	**4**	**5**	**6**	**7**	**8**

The optical losses lie roughly between 6 and 12 dB. It was surprising that the very low values around 2 dB were not present on that chip. This is probably due to the thickness of the reflective gold layer, which was too low. The equipment used for gold sputtering does not allow for an exact thickness measurement but it was possible to observe the transparency of the mirrors by monitoring the reflected optical signal by the mirror and output fiber behind the measured output channel.

A big problem that was encountered on most of the chips was the high variation of the actuation voltage. As previously mentioned, the first actuators switched at 150 V and the last ones switched at 340 V. In

combination with the electromechanical cross talk this invoked the problem that if mirrors with low and high actuation voltage are direct neighbours it was not possible to release the platform with the lower actuation voltage if the platform with high actuation voltage was actuated.

The optical cross talk, which is defined by the amount of light that is coupled into the outgoing fiber having the corresponding mirror in the non-reflective state, was measured to be very low. Typical measurements on good channels showed cross talk of 60 to 80 dB.

5.3.4 Power Consumption

As stated in chapter in chapter 3.3 most of the power that will be used to operate the OXC will be consumed by the load resistance of the high voltage MOSFET switches. A high load resistance is desirable, however, resistances larger than 100 MΩ are not usable if a switching speed of 1 ms is yielded.

During normal operation eight actuators are in the switching state, which means that eight MOSFET switches will be open drawing a current through eight load resistances in parallel.

A picture of the HV step-up converter circuit is shown in figure 5.13. The input power and output voltage for different input voltages were measured and are shown in table 5.5. The load resistance of 10 MΩ was represented by the voltmeter. The conversion efficiency of the circuit lies in the order of only 3%. A higher actuation voltage can be achieved with a higher input voltage at the cost of increased power consumption.

Table 5.5: *Output voltage at load resistance of 10 MΩ. A higher output voltage has the cost of increased power consumption. For a load resistance of 10 MΩ the conversion efficiency is in the order of 3%.*

V_{in} [V]	P_{in} [mW]	V_{out} [V]	Efficiency [%]
5.2	330	329 V	3.28
8.2	480	360 V	2.7
12.0	596	380 V	2.42

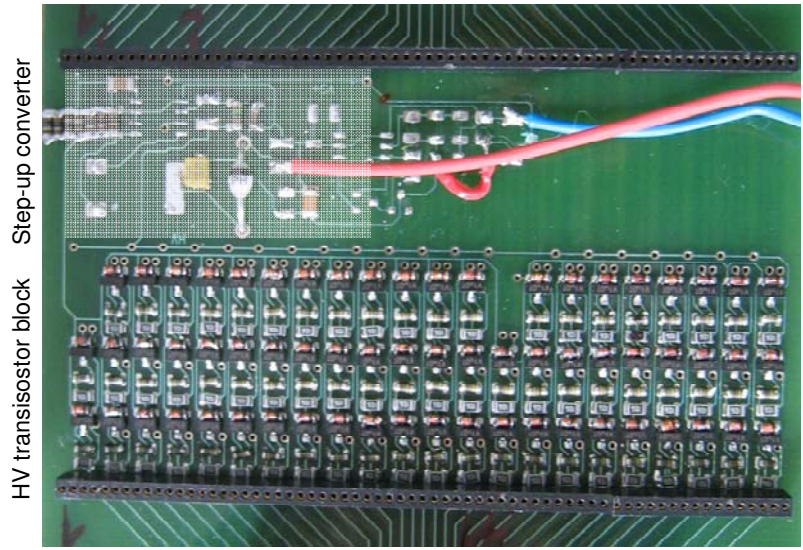

Figure 5.13: *High voltage step-up converter and switching transistor block based on SMD electronics.*

The measurements of output voltage and power consumption for eight load resistances (each measuring 10 MΩ and 100 MΩ) in parallel are given in table 5.6. The power consumption for the case where eight transistors were open is shown in the third column. In the case of load resistances of 10 MΩ the load was too high which resulted in a very unstable behaviour of the voltage converter. Only for the smallest input voltage of 5.2 V could a high voltage be generated. For eight load resistances of 100 MΩ in parallel a high voltage could be generated at similar power consumptions as shown in table 5.5.

In a second experiment eight transistors were actuated at 100 Hz to measure the influence of actuation on the power consumption. For this case, all setups were able to provide a high output voltage. However, for the load resistance of eight times 10 MΩ in parallel a much smaller output voltage was measured, as for the case with only 10 MΩ load. If 100 MΩ resistances were used instead the HV source was able to deliver the desired voltage. The power consumption decreased in comparison to the case where eight transistors were open, which can be explained by the fact that when the transistors are actuated they are closed for 50% of the time and do not draw any current through the load resistors.

The step-up circuit shows a very good performance with 100 MΩ load resistances. The only drawback of a high resistance is a smaller switching speed. The switching time of the circuit was measured to be 0.7 ms, which is sufficient to drive the OXC, where the switching time is 1.5 ms.

Table 5.6: *Output voltage at different load resistances for an 8x8 OXC in operation. Eight times 10 MΩ in parallel is a too high load causing an unstable behaviour of the step-up circuit. The power consumption is lower if the transistors are actuated, which can be explained by the fact that the transistors are closed during 50% of the time.*

Load	**V_{in} [V]**	**$P_{in\ open}$ @ 0 Hz [mW]**	**V_{out} [V]**	**P_{in} @ 100 Hz [mW]**	**V_{out} [V]**
8 x 10 MΩ //	5.2	370	264	276	157
8 x 10 MΩ //	8.2	-	-	395	178
8 x 10 MΩ //	12.0	-	-	376	198
8 x 100 MΩ //	5.2	370	366	321	360
8 x 100 MΩ //	8.2	481	420	455	395
8 x 100 MΩ //	12.0	578	446	512	419

5.3.5 Reliability

Single crystal silicon MEMS are known to be practically unsusceptible to fatigue. Therefore, the monolithic fabrication approach used to fabricate the actuator enables to fabricate very reliable devices. Additionally, the devices are never in mechanical contact, which minimizes the potential risk of failure. Measurements have shown that if the torsion beams have no failure due to the fabrication they do not break during the operation. The actuators of 8x8 matrix were tested for over 9 million switching cycles at 350 volts.

6 Conclusion

The aim of the project leading to this thesis was to create a compact 4x4 and 8x8 optical cross connect for fiber communication. The pitch between the individual mirrors was set to 250 µm to be adapted to the pitch between neighbouring fibers in commercially available fiber ribbons.

The project can be separated into three sub-projects: The MEMS chip, which includes a substantial technology development for its fabrication, the development of the optical components and the assembly of the complete system.

The fabrication of the chips was complex, many fragile pieces had to be fabricated and assembled with very high accuracy, which currently results in a low fabrication yield. However, it was possible to assemble a number of prototypes and to prove the concept. An effort on the fabrication process will have to be done to be able to commercialize the chip in a niche market. This should be possible with the know-how and the technologies achieved during this project. The biggest yield killer on the fabrication side was the fragility of the silicon chips once they were released from the thick Pyrex dummy wafer. Here, a solution has to be found enabling to bond the thin wafer on which the OXC's are fabricated to a silicon wafer. This silicon wafer could serve to fabricate the spacer between mirror matrix and electrode chip and

would provide the desired stability during the fabrication and assembly at the same time.

The fabrication of extremely fragile silicon devices can be achieved by consecutive thermal oxidation and HF vapour phase etching of the SiO_2. The development of a vapour phase etching apparatus allowed the fabrication of torsion beams with length of 150 µm and a diameter of less than 0.5 µm. The potential of the technology is reflected by the large number of projects that now base the release of the microstructures on HF vapour phase etching.

Another inconvenience that was encountered during the testing of the chips was the inhomogeneity of the torsion beams and the resulting variation of the actuation voltage, which most likely originates from the mask tolerances. A better (and unfortunately more expensive) mask for the fabrication of the torsion beams will have to be used for the redesign. A small inhomogeneity of the torsion beams can be tolerated if the switching state of the mirrors is not affected by the electromechanical cross talk.

The electromechanical behaviour of the actuator was simulated by a coupled finite element method as well as by a combined method. For the combined method the capacity of a system was simulated by means of a finite element method (FEM) simulation of the electrostatic energy that is stored the system for the displacements the actuator it thought to move to. This simulation method is very insensitive to the FE model and the mesh that is used, which is not the case for the coupled FEM. The electrostatic force is proportional to the first derivate of the electrostatic energy and is then compared to the mechanical restoring forces of the actuator.

The electromechanical measurements of the actuator agree very well with the simulation results. For a torsion beam diameter of 0.8 µm the actuation voltage was about 300 V.

A big effort was made on the development of micro-optical GRIN-lenses that can be passively aligned to optical fibers and other micro-optical elements on a microchip. The cylindrical lenses have the same diameter as commercially available optical fibers (125 µm) and are placed into a U-groove, which is etched during the same step as the reflective mirrors. This ensures a passive alignment of the microoptical components. The GRIN lenses are diced using a conventional wafer dicing machine and without the need of an expensive clean room environment. The surface roughness on the GRIN lenses is in the order of 1 µm. Optical measurements in index matching oil showed that a negative influence of the surface roughness is not measurable. A collimator setup based on GRIN lenses showed losses of only 0.3 dB and coupling lengths of 2 mm with a loss lower than 2 dB could be achieved. Calculations show that a custom made fiber will achieve coupling

lengths of 8 mm at the same loss. The excellent measurement results make these GRIN lenses a promising candidate for other applications.

The characterisation of the complete system yielded encouraging results. The complex assembly caused that only a low number of switches could be tested. It could be proven that the most important source of optical loss lies in the misalignment of the optical fiber ribbons and the GRIN lenses, which is mostly caused by the fragility of the silicon chip. On the other side, some mirrors showed optical losses that were close to the theoretical loss of the collimator setup itself. Therefore, a process which allows to bond a silicon wafer to the thin wafer containing the mirror matrix will allow the fabrication of mirror arrays yielding a lower loss.

The largest operation frequency in index matching oil was 200 Hz. This value can be raised in the future to 500 Hz with an adapted electronic driving circuit having a smaller load resistance. Nine million switching cycles confirmed the known outstanding mechanical reliability of silicon microstructures.

The innovations presented in this thesis show a very good performance if they are characterized separately and all have a large potential to be integrated into other devices beyond this project. The synthesis of the individual parts to create the desired 8x8 optical cross connect succeeded partially but I am very confident that the high aims can be reached in the future.

Acknowledgements

I would like to acknowledge all the people who contributed to the realization of my thesis, especially Prof. Nico de Rooij who gave me the opportunity to work within his group where I obtained all the freedom I needed to accomplish my thesis. Furthermore, I thank my advisor Wilfried Noell and the other members of the OMEMS group for their fruitful collaboration, namely Yves Petremand, Thomas Overstolz, Winston Sun, and Severin Waldis.

I thank Cornel Marxer, the manager of Sercalo Inc., and the rest of the Sercalo team for initiating the project and for supporting my work.

I am grateful to the whole SAMLAB team, Edith Millotte, Gianni Mondin, Nicole Hegelbach, Sylvain Jeanneret, Sylviane Pochon, Jose Vaquera, Stephan Ischer, and Pierre-Andre Clerc, for teaching me the mysteries of the cleanroom, supporting my ideas and the great work they did on the project. Furthermore, I want to thank Peter van der Wal to be my private chemist and Claudio Novelli for the IT infrastructure.

A great experience was the collaboration with students Peter Veltmann, Alex Oudalov, Samuel Hoffmann and the fellow Peter Herbst who all contributed a piece to the big puzzle.

Last but not least I want to thank all the other members of the SAMLAB for the discussions and the time we spent in addition to the work.

Biography

Michael Zickar was born on the 15th of February 1977 in Pompaples, VD, Switzerland. He spent primary and secondary school in Aarburg and high school in Zofingen where he visited the scientific department. From 1997 to 2002 he studied Physical Electronics at the University of Neuchatel. The Master Thesis was done in 2002 at the Institute of Industrial Science at the University of Tokyo. Under the direction of Prof. Fujita he dealt with the design, analysis, fabrication and evaluation of electrostatic vertical comb drive actuators. He received the Diploma in Physical Electronics at the University of Neuchatel, Switzerland in 2002.

In May 2002 he joined the Sensors and Microactuator Laboratory at the University of Neuchatel for a PhD thesis in which he was developing optical cross connects and microoptical elements under the direction of Wilfried Noell and Nico de Rooij. Currently he is developing MEMS for medical devices. In 2004 he co-founded Idonus Sarl., which is a company specialized in fabricating instruments for wet- and vapor phase etching apparatuses for microfabrication.

Publication List

Yves Salvade, Rene Dandliker, Michael Zickar, “Air dispersion measurement by second harmonic interferometry”, Proc. of SPIE, Optics Letters, 2002, Vol. 27, No. 16, pp. 1424-6.

Michael Zickar, Wilfried Noell, Cornel Marxer, Nico de Rooij, “4x4 & 8x8 Optical Cross connect for Fiber Optical Networks”, Proc. of SPIE, vol. 5455, Photonics Europe 04, Strasbourg, France, pp. 212-219.

Michael Zickar, Wilfried Noell, Alex Oudalov, Cornel Marxer, Nico de Rooij, “4x4 & 8x8 Optical Matrix Switch with 250 µm Mirror Pitch”, OMEMS 04, Takamatsu, Japan, pp. 162-163.

Thomas Overstolz, Pierre-Andre Clerc, Wilfried Noell, Michael Zickar, Nico de Rooij, “A clean wafer-scale chip-release process without dicing based on vapor phase etching”, MEMS 2004, Maastricht, The Nederlands, pp. 717-720.

Michael Zickar, Alex Oudalov, Wilfried Noell, Cornel Marxer, Nico de Rooij, “MEMS compatible Micro-GRIN Lenses for in Plane Beam Manipulation”, OMEMS 05, Oulu, Finnland, pp. 111-112.

Michael Zickar, Wilfried Noell, Thomas Overstolz, Christian Spörl, Nico de Rooij, “Quasi-dry Release for Micro Electro-Mechanical Systems”, conference proc., COMS 2005, Baden-Baden, Germany, pp. 611-616.

Severin Waldis, Pierre-Andre Clerc, Frederic Zamkotsian, Michael Zickar, Wilfried Noell, Nico de Rooij, “High-fill factor micro-mirror array for multi object spectroscopy”, Proc. of SPIE, Vol. 6114, Photonics West 2006.

International Patent Application: “Optical Coupling Element and Method of Manufacturing the Optical Coupling Element“, PCT/IB2004/001611.

Patent Application: “Shutter device for pixel element and pixel arrangement”, Application No. 05003576.5-

Rogier Receveur, Michael Zickar, Cornel Marxer, Vincent Larik, Nico de Rooij, “Wafer level hermetic package and device testing of SOI-MEMS switch for biomedical applications”, J. Micromech. Microeng. 16 (2006) 676-683.